H2O and O2 absorption in the coma of comet 67P/Churyumov–Gerasimenko measured by the Alice far-ultraviolet spectrograph on Rosetta

Brian A. Keeney, S. Alan Stern, Michael F. A'Hearn, Jean-Loup Bertaux, Lori M. Feaga, Paul D. Feldman, Richard A. Medina, Joel Wm. Parker, Jon P. Pineau, Eric Schindhelm, et al.

Monthly Notices of the ROYAL ASTRONOMICAL SOCIETY

MNRAS **469,** S158–S177 (2017)
Advance Access publication 2017 June 8

doi:10.1093/mnras/stx1426

H_2O and O_2 absorption in the coma of comet 67P/Churyumov–Gerasimenko measured by the Alice far-ultraviolet spectrograph on *Rosetta*

Brian A. Keeney,[1★] S. Alan Stern,[1] Michael F. A'Hearn,[2] Jean-Loup Bertaux,[3] Lori M. Feaga,[2] Paul D. Feldman,[4] Richard A. Medina,[1] Joel Wm. Parker,[1] Jon P. Pineau,[5] Eric Schindhelm,[1] Andrew J. Steffl,[1] M. Versteeg[6] and Harold A. Weaver[7]

[1] *Southwest Research Institute, Department of Space Studies, Suite 300, 1050 Walnut Street, Boulder, CO 80302, USA*
[2] *Department of Astronomy, University of Maryland, College Park, MD 20742, USA*
[3] *LATMOS, CNRS/UVSQ/IPSL, 11 Boulevard d'Alembert, F-78280 Guyancourt, France*
[4] *Department of Physics and Astronomy, Johns Hopkins University, 3400 N. Charles Street, Baltimore, MD 21218, USA*
[5] *Stellar Solutions, Inc., 250 Cambridge Ave., Suite 204, Palo Alto, CA 94306, USA*
[6] *Southwest Research Institute, 6220 Culebra Road, San Antonio, TX 78238, USA*
[7] *Johns Hopkins University Applied Physics Laboratory, 11100 Johns Hopkins Road, Laurel, MD 20723, USA*

Accepted 2017 June 5. Received 2017 June 5; in original form 2017 April 14

ABSTRACT

We have detected H_2O and O_2 absorption against the far-UV continuum of stars located on lines of sight near the nucleus of Comet 67P/Churyumov–Gerasimenko using the Alice imaging spectrograph on *Rosetta*. These stellar appulses occurred at impact parameters of $\rho = 4$–20 km, and heliocentric distances ranging from $R_{\rm h} = -1.8$ to 2.3 au (negative values indicate pre-perihelion observations). The measured H_2O column densities agree well with nearly contemporaneous values measured by VIRTIS-H. The clear detection of O_2 independently confirms the initial detection by the ROSINA mass spectrometer; however, the relative abundance of O_2/H_2O derived from the stellar spectra (11–68 per cent, with a median value of 25 per cent) is considerably larger than published values found by ROSINA. The cause of this difference is unclear, but potentially related to ROSINA measuring number density at the spacecraft position while Alice measures column density along a line of sight that passes near the nucleus.

Key words: comets: individual: 67P – ultraviolet: planetary systems.

1 INTRODUCTION

One of the most significant results from the *Rosetta* mission to Comet 67P/Churyumov–Gerasimenko (67P/C–G) has been the persistent detection of O_2 in the coma (Bieler et al. 2015; Fougere et al. 2016) by the double-focusing mass spectrometer (DFMS) of the Rosetta Orbiter Spectrometer for Ion and Neutral Analysis (ROSINA; Balsiger et al. 2007). The initial detection by Bieler et al. (2015) found that the relative number density of O_2 with respect to H_2O ranged from 1–10 per cent, with a mean of $n_{O_2}/n_{H_2O} = 3.85 \pm 0.85$ per cent for measurements taken between 2014 September and 2015 March. Further modelling by Fougere et al. (2016) found that the relative production rate of O_2 with respect to H_2O is ≈1–2 per cent for measurements taken prior to 2016 February. Both studies find that the number densities of O_2 and H_2O are highly correlated, with Pearson correlation coefficients >0.8.

Surprisingly, O_2 is the fourth most abundant species in the coma of 67P/C–G (behind H_2O, CO_2 and CO; Le Roy et al. 2015; Fougere et al. 2016), despite the fact that it had never been detected in a cometary coma before (Bieler et al. 2015). Subsequent reanalysis of mass spectrometer data from *Giotto*'s visit to Oort-Cloud Comet 1P/Halley has found that $n_{O_2}/n_{H_2O} = 3.7 \pm 1.7$ per cent is consistent with the measurements (Rubin et al. 2015), suggesting that O_2 may be a common constituent of all comets, not just Jupiter Family Comets such as 67P/C–G. New theories are being developed to explain these O_2 detections, such as trapping O_2 in clathrates prior to agglomeration during comet formation (Mousis et al. 2016), astrochemical production of O_2 in dark clouds or forming protoplanetary discs (Taquet et al. 2016) and formation of O_2 during the evaporation of H_2O ice via dismutation of H_2O_2 (Dulieu, Minissale & Bockelée-Morvan 2017).

★ E-mail: bkeeney@gmail.com

In this Paper, we present H_2O and O_2 column densities measured along lines of sight to background stars projected near the nucleus of 67P/C–G by the Alice far-UV spectrograph (Stern et al. 2007). These stellar sight lines allow the coma of 67P/C–G to be studied in far-UV absorption, where column densities can be measured directly. Alice's previous characterizations of the coma of 67P/C–G have primarily used emission lines from CO and atomic hydrogen, oxygen, carbon and sulphur (e.g. Feldman et al. 2015, 2016). While the strengths of these emission lines can only be used to derive molecular column densities under specific assumptions (i.e. pure resonance fluorescence), the ratios of strong, commonly observed lines can be diagnostic of physical conditions in the coma. Feldman et al. (2016) inferred that O_2 was the primary driver of certain gaseous outbursts that exhibit a sudden increase in the O I $\lambda1356/\lambda1304$ ratio in the sunward coma without any corresponding increase in dust production. Feldman et al. (2016) estimate that $O_2/H_2O \geq 50$ per cent during these outbursts, substantially higher than the mean value of 3.85 ± 0.85 per cent found by Bieler et al. (2015).

Several of *Rosetta*'s instruments are capable of measuring the abundance of H_2O (as well as CO and CO_2) in the coma of 67P/C–G. Most notably, ROSINA measures the number density of water, n_{H_2O}, at the spacecraft location using mass spectroscopy, while the Visible and Infrared Thermal Imaging Spectrometer (VIRTIS; Coradini et al. 2007) and the Microwave Instrument for the Rosetta Orbiter (Gulkis et al. 2007) measure the column density of water, N_{H_2O}, along a specific line of sight using rotational and/or vibrational transitions. The UV-absorption spectra presented herein also allow Alice to directly measure N_{H_2O}, and facilitate comparisons with nearly contemporaneous measurements from ROSINA (Fougere et al. 2016) and VIRTIS-H (the high spectral resolution channel of VIRTIS; Bockelée-Morvan et al. 2016).

In contrast to the situation with H_2O, only Alice and ROSINA are capable of directly measuring O_2. This makes the observations reported herein an important and unique confirmation of the initial O_2 detections (Bieler et al. 2015). However, direct comparisons between ROSINA's *in situ* measurements and Alice's measurements along specific lines of sight are not straightforward. The remainder of this Paper is organized as follows: the Alice spectrograph and stellar spectra are described in Section 2; H_2O and O_2 column densities are derived in Section 2; our values are compared with ROSINA and VIRTIS-H measurements in Section 3; and our conclusions are presented in Section 4.

2 STELLAR APPULSE OBSERVATIONS

Alice is a low-power, lightweight far-UV imaging spectrograph funded by NASA for inclusion on the ESA *Rosetta* orbiter (Stern et al. 2007). It covers the wavelength range 750–2050 Å with a spectral resolution of 8–12 Å, and has a slit that is 6° long, and narrower in the centre (0°.05 wide) than the edges (0°.1 wide; Stern et al. 2007). Over the course of *Rosetta*'s orbital escort mission, Alice probed the sunward coma of 67P/C–G in absorption 30 times using UV-bright stars located along lines of sight near the nucleus as background sources. Here we report on the 29 observations ('appulses') that were not occulted by the nucleus; we will report the details of our single stellar occultation separately (B. Keeney et al., in prep).

Quantifying the nature of the cometary coma required re-observing, or 'revisiting', these stars when they were far from the nucleus to characterize their intrinsic stellar spectra. This allowed us to isolate the coma absorption signature from the combined background effects of the stellar continuum and interstellar absorption. Further, there are two varieties of appulse observations, which we term 'targeted' and 'archival' appulses.

For the targeted appulses, we actively searched during operations planning for upcoming opportunities where a known bright star would be located within a few degrees of the nucleus. Inertial pointings were designed that facilitated long stares at these stars during the appulses, at the expense of a time-varying distance to the nucleus over the course of each observation. These targeted appulses were observed between 2015 December 25 and 2016 February 1 at heliocentric distances of $R_h = 1.97$–2.26 au, and are characterized by long exposure times (typically 12 Alice spectral images with exposure times of 10–20 min each were obtained per appulse), large off-nadir angles ($\theta \approx 5$–$10°$), and large R_h compared to their archival counterparts.

To complement the targeted appulses, we also searched the extensive Alice archive (~40 000 exposures include the nucleus in the field of view) for instances where we serendipitously observed a UV-bright star near the nucleus as part of normal operations. This search returned hundreds of candidates that were prioritized by the star's brightness and proximity to the nucleus, as well as the duration of the appulse and its proximity to the comet's perihelion passage on 2015 August 12, when coma activity was near its peak (Fougere et al. 2016). Since our typical pointing during normal operations was fixed with respect to the nucleus (i.e. not an inertial reference frame), we do not know the exact duration of the archival appulses because the star is moving with respect to the slit; however, we can estimate their durations with uncertainties of ~10 per cent using Navigation and Ancillary Information Facility SPICE (Acton 1996). The archival appulses were observed between 2015 April 29 and 2015 December 26 at $R_h = 1.24$–1.98 au, and typically have shorter durations (10–20 min), smaller off-nadir angles ($\theta < 5°$), and smaller R_h than their targeted counterparts. However, the smaller off-nadir angles for the archival appulses are somewhat counteracted by the large spacecraft-comet distance, Δ, near perihelion, which led to similar impact parameters ($\rho = \Delta \sin\theta \approx 5$–$20$ km) for all appulses.

Tables 1 and 2 list the properties of the seven targeted and 22 archival appulses, respectively. The following information is listed by column: (1) the name of the star; (2) the stellar type and luminosity class as listed by SIMBAD (Wenger et al. 2000); (3) the observation type (either 'appulse' or 'revisit'); (4) the date of observation; (5) the total exposure time, in minutes; (6) the heliocentric distance, R_h, in au, where negative values indicate that the observation occurred prior to perihelion on 2015 August 12; (7) the phase angle, ϕ, in degrees; (8) the off-nadir angle, θ, in degrees; and (9) the impact parameter, ρ, in km. The impact parameter is only listed for appulse observations, not revisits, and the entries are ordered by appulse date.

Appulse observations have small off-nadir angles by construction ($\theta = 0°$ implies we are looking straight at the nucleus), and revisits were constrained to have $\theta > 30°$, although most were acquired when $\theta > 90°$. Most of the appulses and revisits were observed at $\approx 90°$ phase, with occasional deviations up to $\pm 30°$ from this value. Note that one of the targeted stars, HD 40111, has two distinct appulses separated by ~2 weeks (see Table 1).

All exposures for a given appulse or revisit were flux-calibrated using spectrophotometric standard stars. Stellar spectra were then extracted from the spectral images and background subtracted. Spectra extracted from individual exposures were combined to improve the signal-to-noise ratio after first being normalized to have the same median flux from 1800–1900 Å. This range was chosen

Table 1. Journal of Targeted Stellar Appulse observations.

Star	Sp. type	Obs. type	Date	UTC	Duration (min)	R_h (au)	ϕ (°)	θ (°)	ρ (km)
HD 140008	B5 V	Appulse	2015 December 25	14:27:11	57	1.97	89.8	4.8–5.3	6.4–7.2
–	–	Revisit 1	2016 February 29	–	37	2.47	92.9	88.3–88.9	–
–	–	Revisit 2	2016 March 12	–	39	2.56	91.9–92.0	87.0–88.0	–
HD 144294	B2.5 V	Appulse	2015 December 25	15:37:11	111	1.97	89.8	9.9–10.8	13.3–14.6
–	–	Revisit	2016 March 4	–	127	2.51	91.8	120.0–123.8	–
HD 42933	B1/2 III	Appulse	2016 January 10	07:19:29	164	2.09	89.6	5.1–6.5	7.0–8.9
–	–	Revisit 1	2016 February 29	–	51	2.47	92.9	171.1–171.8	–
–	–	Revisit 2	2016 February 29	–	77	2.48	92.6	172.9–173.8	–
HD 89890	B5 II	Appulse	2016 January 18	13:28:59	169	2.16	60.4–60.5	12.1–12.9	17.1–18.2
–	–	Revisit	2016 March 15	–	84	2.59	89.1	145.3–148.4	–
HD 40111	B0/1 II/III	Appulse 1	2016 January 25	17:32:33	222	2.21	60.2–60.4	11.4–12.5	14.0–15.4
–	–	Appulse 2	2016 February 9	19:38:27	170	2.33	64.9–65.6	8.8–9.8	7.8–8.6
–	–	Revisit 1	2016 February 23	–	131	2.43	89.2–90.1	120.4–122.3	–
–	–	Revisit 2	2016 February 26	–	88	2.45	94.8	171.2–172.0	–
HD 144206	B9 III	Appulse	2016 February 1	13:28:59	170	2.26	60.2–60.4	9.8–9.9	10.0–10.1
–	–	Revisit	2016 April 1	–	62	2.71	112.1–112.9	177.8–178.7	–

Notes. The phase angle is denoted by ϕ and the off-nadir angle by θ. The last column lists the impact parameter, ρ.

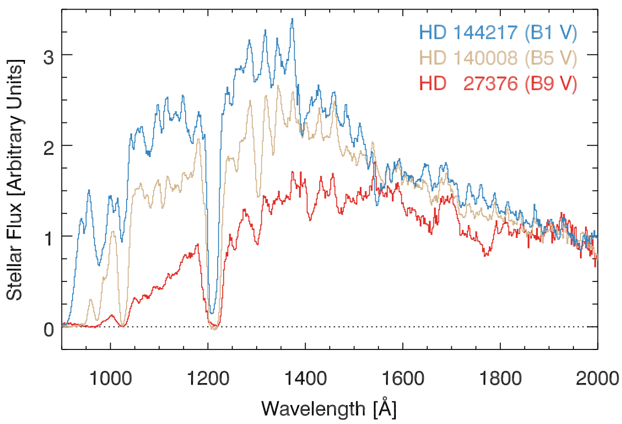

Figure 1. Revisit spectra for three main sequence stars. The spectra are normalized to have the same flux from 1800–1900 Å to emphasize the differences between early- and late-type *B* stars at far-UV wavelengths.

because both H_2O and O_2 have very small absorption cross-sections in this region (Chung et al. 2001; Yoshino et al. 2005), but the stellar spectra still have sufficient signal to noise to allow a robust flux measurement (the effective area of Alice decreases rapidly for wavelengths >1800 Å; Stern et al. 2007).

Next, the co-added revisit spectrum was scaled to have the same median flux from 1800–1900 Å as the co-added appulse spectrum. Finally, the appulse spectrum was divided by the scaled revisit (i.e. unocculted) spectrum to create a normalized spectrum in which the intrinsic stellar flux and interstellar absorption have been removed and only the differences in foreground coma absorption between the appulse and revisit spectra remain. By normalizing the spectra in this manner we also make ourselves insensitive to the uncertainty in the amount of time the star was in the slit.

Fig. 1 displays co-added revisit spectra for three main sequence stars that span the range of stellar types observed. All three stars have sufficient flux at $\lambda > 1400$ Å to create normalized spectra with reasonable signal to noise, but the early- and mid-type *B* stars have considerably more flux at shorter wavelengths than the late-type *B* stars do. Thus, normalized spectra for late-type appulse stars are inherently noisier at bluer wavelengths than normalized spectra for earlier-type stars.

We note that in a few cases we normalized the spectra from 1400–1450 Å when normalization from 1800–1900 Å was problematic. While 1400–1450 Å has small H_2O absorption cross-sections (Chung et al. 2001), it is the region where O_2 absorption cross-sections are largest (Yoshino et al. 2005). The 1400–1450 Å region is therefore not ideal for spectral normalization, since using it reduces our sensitivity for O_2 absorption. Fits to spectra where we had to use this normalization region are not used for detailed analyses.

We have searched for optically-thin absorption from H_2O and O_2 in the normalized stellar spectra as described above. For a given molecule, *i*, we model the optical depth, τ_i, as a function of wavelength, λ, as

$$\tau_i(\lambda) = N_i\,\sigma_i(\lambda), \tag{1}$$

where N_i is the column density of species *i* and $\sigma_i(\lambda)$ is the absorption cross-section of species *i* as a function of wavelength. Combining absorption from several different species yields an expected (normalized) model flux of

$$F(\lambda) = \mathrm{e}^{-\sum \tau_i(\lambda)}. \tag{2}$$

This model spectrum can then be compared to the normalized stellar spectrum to constrain the column densities of interest.

Table 3 lists the ten species that we model in our analysis. While we are primarily interested in H_2O and O_2, other abundant species must be included to robustly constrain the range of permissible H_2O and O_2 column densities. All species with >0.5 per cent abundance relative to H_2O in the coma of 67P/C–G in Le Roy et al. (2015) with available far-UV absorption cross-sections are tabulated. Table 3 lists the following information by column: (1) species; (2) wavelength range; (3) measurement temperature; and (4) measurement reference. The adopted cross-sections were downloaded from the PHoto Ionization/Dissociation RATES website[1] (Huebner & Mukherjee 2015); for most species, they are composites of several different measurements covering the wavelength range 900–2000 Å. The molecular cross-sections in Table 3 are displayed in Fig. 2.

[1] http://phidrates.space.swri.edu

Table 2. Journal of Archival Stellar Appulse observations.

Star	Sp. type	Obs. type	Date	UTC	Duration (min)	R_h (au)	ϕ (°)	θ (°)	ρ (km)
HD 26912	B3 IV	Appulse	2015 April 30	02:00:27	18	−1.75	72.5–72.6	1.7	4.5
–	–	Revisit	2016 March 26	–	95	2.67	128.7–131.5	77.7–80.0	–
HD 3901	B2 V	Appulse	2015 May 3	21:32:21	11	−1.72	60.3	1.7	4.0
–	–	Revisit	2016 August 5	–	12	3.52	–	44.9	–
HD 29589	B8 IV	Appulse	2015 May 27	03:19:43	46	−1.55	65.9	1.3	7.1
–	–	Revisit	2016 July 22	–	24	3.44	88.8	99.0	–
HD 174585	B3 IV	Appulse	2015 June 8	00:40:54	16	−1.48	87.4	1.5	5.4
–	–	Revisit	2016 August 5	–	12	3.52	90.1	92.9	–
HD 180554	B4 IV	Appulse	2015 June 28	00:16:04	4	−1.36	89.2	2.4	7.7
–	–	Revisit	2016 August 5	–	12	3.52	92.6	96.9	–
HD 191692	B9.5 III	Appulse	2015 July 12	22:59:29	14	−1.30	88.8	2.5	6.8
–	–	Revisit	2016 April 19	–	17	2.84	86.4	35.2	–
HD 195810	B6 III	Appulse	2015 July 25	08:56:47	11	−1.26	90.0	2.0	6.5
–	–	Revisit	2016 April 19	–	17	2.84	86.5	41.1	–
HD 192685	B3 V	Appulse	2015 July 26	08:54:44	11	−1.26	89.9	2.5	7.4
–	–	Revisit	2016 June 27	–	17	3.29	93.8	99.9	–
HD 68324	B2 V	Appulse	2015 August 9	19:39:33	20	−1.24	89.0	1.3	7.0
–	–	Revisit	2016 June 6	–	30	3.15	67.9–68.2	88.2–88.4	–
HD 66006	B2/3	Appulse	2015 August 10	04:28:49	21	−1.24	89.0	1.0	5.7
–	–	Revisit	2016 June 6	–	31	3.15	69.1–69.5	86.6–87.0	–
HD 64722	B2 IV	Appulse	2015 August 10	18:45:04	25	−1.24	89.2	2.5	14.2
–	–	Revisit	2016 June 27	–	21	3.29	93.8	47.7–48.1	–
HD 39844	B6 V	Appulse	2015 August 13	00:57:11	14	1.24	89.3	2.2	12.6
–	–	Revisit	2016 June 27	–	17	3.29	93.8	35.4	–
HD 207330	B3 III	Appulse	2015 August 27	03:18:10	12	1.26	79.7	1.5	10.4
–	–	Revisit	2016 April 4	–	116	2.67	83.1–83.3	149.5–150.8	–
HD 109387	B6 III	Appulse	2015 September 1	07:04:57	10	1.27	70.4	1.2	8.6
–	–	Revisit	2016 June 5	–	22	3.15	85.3–85.6	135.2–135.7	–
HD 124771	B3 V	Appulse	2015 September 10	04:52:33	12	1.29	119.9	3.6	20.1
–	–	Revisit	2016 June 6	–	18	3.15	68.8	50.0	–
HD 21428	B3 V	Appulse	2015 November 2	16:07:12	10	1.58	60.2	2.8	12.8
–	–	Revisit	2016 August 5	–	12	3.52	94.9	28.2	–
HD 32249	B3 IV	Appulse	2015 November 6	06:42:59	9	1.60	61.3	2.6	10.7
–	–	Revisit	2016 July 22	–	9	3.44	88.9	77.1	–
HD 33328	B2 IV	Appulse	2015 November 6	09:41:26	4	1.60	61.6	1.4	5.9
–	–	Revisit	2016 July 22	–	9	3.44	88.7	81.6	–
HD 106625	B8 III	Appulse	2015 November 13	08:16:25	6	1.65	61.1	1.6	4.7
–	–	Revisit	2016 July 22	–	24	3.44	89.1	70.7	–
HD 27376	B9 V	Appulse	2015 November 27	22:04:50	8	1.76	90.0	3.4	8.1
–	–	Revisit	2016 July 22	–	14	3.44	88.9	48.7	–
HD 23466	B3 V	Appulse	2015 December 16	22:38:45	7	1.90	89.8	2.9	5.2
–	–	Revisit	2016 August 2	–	12	3.51	78.5	60.3	–
HD 144217	B1 V	Appulse	2015 December 26	06:30:02	8	1.98	89.8	3.2	4.4
–	–	Revisit	2016 August 5	–	12	3.52	91.5	130.4	–

Notes. The phase angle is denoted by ϕ, and the off-nadir angle by θ. The last column lists the impact parameter, ρ.

All of the cross-section measurements were performed near room temperature and laboratory measurements are not consistently available for all species in Table 3 at any other temperature; however, the gas kinetic temperature in the coma of 67P/C–G varies considerably. Barucci et al. (2016) found that exposed water ice on the nucleus has $T \approx 160$–220 K, while Lee et al. (2015) found that the temperature of the coma decreases as $T \propto \rho^{-1}$ until it reaches a terminal temperature of $T \approx 50$–75 K. The discrepancy between the temperature of the gas whose cross-section was measured and the temperature of the absorbing coma gas introduces a systematic uncertainty in our model column densities that is not quantified by our modelling procedure. The peak O_2 cross-section decreases by ∼0.1 dex as the temperature decreases from 295 to 78 K (Yoshino et al. 2005); thus, by assuming room-temperature cross-sections we are systematically under-estimating the O_2 column density required to match the observed absorption. Unfortunately, no H_2O cross-sections are available at $T < 250$ K, so we are unable to estimate the magnitude of the systematic variation in O_2/H_2O.

We estimate the molecular column densities using non-linear least-squares regression of equation (2) with MPFIT[2] (Markwardt 2009). The free parameters of the fit are the logarithm of the H_2O column density, in units of cm^{-2}, and the relative column densities of O_2, CO, CO_2 etc. with respect to water (e.g. $O_2/H_2O \equiv N_{O_2}/N_{H_2O}$). The O_2, CO and CO_2 columns are constrained to lie in the range of 0–100 per cent relative to H_2O, and all other species are

[2] http://purl.com/net/mpfit

Table 3. Molecular cross-sections.

Species	λ (Å)	T (K)	Reference
H_2O	1400–1898	250	Chung et al. (2001)
–	1148–1939	298	Mota et al. (2005)
–	850–1110	298	Watanabe & Jursa (1964)
–	1060–1860	298	Watanabe & Zelikoff (1953)
O_2	1300–1752	295	Yoshino et al. (2005)
–	41–1771	298	Brion & Tan (1979)
–	1163–2000	298	Ackerman, Biaume & Kockarts (1970)
CO	584–1038	298	Cairns & Samson (1965)
CO_2	1061–1187	295	Stark et al. (2007)
–	1187–1755	295	Yoshino et al. (1996)
–	61–1450	298	Chan, Cooper & Brion (1993)
–	155–1550	298	Hitchcock, Brion & van der Wiel (1980)
CH_4	1380–1600	295	Mount & Moos (1978)
–	952–1306	295	Sun & Weissler (1955)
–	773–1370	298	Ditchburn (1955)
C_2H_2	1050–2011	298	Nakayama & Watanabe (1964)
–	600–1000	298	Metzger & Cook (1964)
C_2H_6	1380–1600	295	Mount & Moos (1978)
–	1200–1380	298	Okabe & Becker (1963)
–	1160–1200	298	Lombos, Sauvageau & Sandorfy (1967)
–	354–1127	–	Koch & Skibowski (1971)
C_2H_4	500–1200	–	Schoen (1962)
–	1065–1960	–	Zelikoff & Watanabe (1953)
C_4H_2	1210–1730	296	Okabe (1981)
–	1600–2600	295	Fahr & Nayak (1994)
H_2CO	600–1760	–	Mentall et al. (1971)
–	1760–1850	–	Gentieu & Mentall (1970)

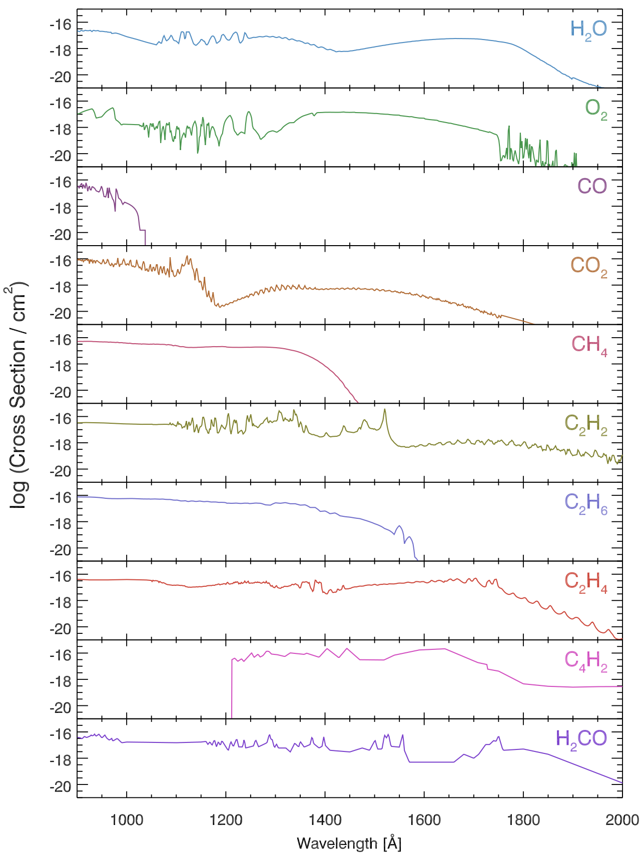

Figure 2. Molecular absorption cross-sections used in this work.

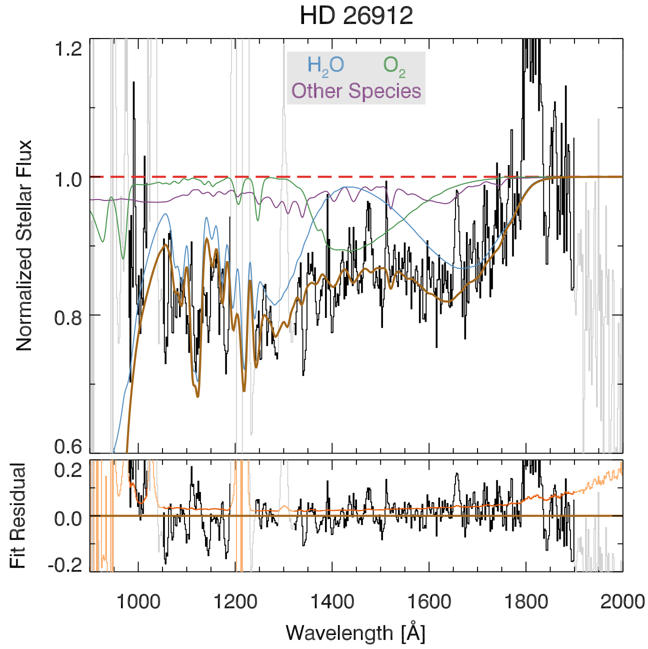

Figure 3. Fits to the appulse absorption of HD 26912 (FQ = 2). Top: the normalized stellar flux (black) with best-fitting ensemble absorption (brown) overlaid. Individual absorption from H_2O (blue), O_2 (green), and other species (purple; ensemble sum of CO, CO_2, CH_4 etc. from Table 3) are also shown. Bottom: the residual of the ensemble fit, with 1σ flux uncertainty (orange) overlaid. Masked regions are shown in lighter hues in both panels; these regions are not used to constrain the fits. Absorption fits for all targeted and archival stellar appulses are shown in Appendix A.

constrained to the range 0–1 per cent. We model the wavelength range 950–1900 Å, with regions near strong coma emission lines (e.g. H I Ly α, H I Ly β, and the O I 1304 Å multiplet, where residuals from background subtraction are often present) and regions with very low S/N masked out. The fit to the appulse of HD 26912 is presented in Fig. 3, which shows the normalized stellar spectrum compared to ensemble and individual-species absorption in the top panel and the ensemble fit residual in the bottom panel. Fits to all targeted and archival appulses are presented in Appendix A.

The best-fitting values of log N_{H_2O} and O_2/H_2O for all of the stellar appulses are shown in Table 4, which lists the following information by column: (1) star name; (2) median S/N in the wavelength range 1250–2000 Å; (3) Fit Quality (FQ) flag; (4) logarithm of the best-fitting H_2O column density, in cm^{-2}; (5) best-fitting value of the relative column density of O_2 relative to H_2O; (6) logarithm of the adopted H_2O column density, in cm^{-2}; and (7) adopted value of the relative column density of O_2 relative to H_2O. The 'adopted' values in Columns 6 and 7 are described in more detail in Section 2.1. All quantities in Columns 4–7 are listed with 1σ uncertainties.

The FQ flag in Column 3 is a subjective measure of the quality of the absorption line fit for a given star, with lower values indicating higher quality. Stars with FQ = 1 are reasonably fit over the full wavelength range 900–2000 Å (see Fig. A8). Stars with FQ = 2 have some regions of very low S/N (see Fig. A6), or mild discrepancies between the observed and model fluxes (see Fig. A3). Stars with FQ = 3 have large regions with systematic discrepancies between the observed and model fluxes. All stars that were normalized from 1400–1450 Å instead of the default 1800–1900 Å region (see Section 2) were assigned FQ = 4. We also assigned

Table 4. Stellar Appulse Column Densities.

Star	S/N	FQ	Best-fitting values log N_{H_2O}	Best-fitting values O_2/H_2O	Adopted values log N_{H_2O}	Adopted values O_2/H_2O
HD 26912	33	2	16.40 ± 0.01	0.327 ± 0.024	16.40 ± 0.04	0.315 ± 0.056
HD 3901	19	4	16.16 ± 0.02	0.000	16.14 ± 0.09	<0.179
HD 29589	48	2	17.03 ± 0.01	0.442 ± 0.015	17.03 ± 0.03	0.435 ± 0.046
HD 174585	17	3	16.49 ± 0.02	0.038 ± 0.021	16.49 ± 0.06	<0.155
HD 180554	13	4	16.37 ± 0.03	0.000	16.36 ± 0.09	<0.164
HD 191692	28	2	16.76 ± 0.01	0.123 ± 0.009	16.76 ± 0.04	0.123 ± 0.035
HD 195810	27	2	16.80 ± 0.01	0.223 ± 0.013	16.80 ± 0.04	0.219 ± 0.040
HD 192685	30	1	16.75 ± 0.01	0.087 ± 0.014	16.75 ± 0.04	<0.123
HD 68324	45	2	16.85 ± 0.01	0.161 ± 0.016	16.85 ± 0.03	0.155 ± 0.042
HD 66006	39	1	17.08 ± 0.01	0.111 ± 0.009	17.08 ± 0.03	0.109 ± 0.030
HD 64722	37	2	16.76 ± 0.01	0.324 ± 0.015	16.76 ± 0.03	0.321 ± 0.044
HD 39844	14	2	16.73 ± 0.01	0.188 ± 0.013	16.72 ± 0.05	0.190 ± 0.048
HD 207330	39	2	16.80 ± 0.01	0.150 ± 0.010	16.80 ± 0.04	0.149 ± 0.033
HD 109387	27	1	16.78 ± 0.01	0.154 ± 0.013	16.78 ± 0.04	0.151 ± 0.041
HD 124771	24	1	16.56 ± 0.01	0.288 ± 0.017	16.55 ± 0.04	0.285 ± 0.049
HD 21428	20	4	15.81 ± 0.03	0.000	15.82 ± 0.12	<0.272
HD 32249	28	2	16.50 ± 0.01	0.569 ± 0.025	16.50 ± 0.04	0.560 ± 0.066
HD 33328	25	2	16.47 ± 0.01	0.128 ± 0.023	16.46 ± 0.04	<0.167
HD 106625	49	1	16.72 ± 0.01	0.309 ± 0.009	16.72 ± 0.04	0.308 ± 0.031
HD 27376	23	3	16.18 ± 0.03	0.000	16.16 ± 0.09	<0.145
HD 23466	15	4	16.07 ± 0.04	0.000	16.06 ± 0.11	<0.224
HD 140008	49	2	15.95 ± 0.03	0.355 ± 0.048	15.94 ± 0.06	0.334 ± 0.072
HD 144294	102	3	15.63 ± 0.02	0.590 ± 0.069	15.61 ± 0.05	0.563 ± 0.089
HD 144217	53	3	16.00 ± 0.03	0.000	15.98 ± 0.08	<0.116
HD 42933	119	3	15.60 ± 0.02	0.441 ± 0.050	15.58 ± 0.05	0.412 ± 0.081
HD 89890	62	4	15.33 ± 0.04	1.000	15.30 ± 0.11	>0.733
HD 40111 (A)	86	3	15.59 ± 0.02	0.702 ± 0.053	15.57 ± 0.06	0.678 ± 0.089
HD 144206	35	2	15.80 ± 0.03	0.521 ± 0.056	15.78 ± 0.08	0.495 ± 0.092
HD 40111 (B)	76	3	15.27 ± 0.04	0.297 ± 0.060	15.18 ± 0.12	<0.338

Notes. Entries are ordered chronologically and all column densities have units of cm^{-2}.
Uncertainties are quoted at the 1σ level and limits are quoted at the 3σ level.

FQ = 4 to the appulse of HD 89890, whose fit preferred $N_{O_2} > N_{H_2O}$ and had systematic discrepancies throughout the fitting range. Only stars with FQ ≤ 3 are used in subsequent analyses.

There are two notable features of the best-fitting column densities in Table 4. The first is that the formal fitting uncertainties are very small. The second is that the O_2/H_2O values are considerably higher than those in Bieler et al. (2015), who found a mean value of 3.85 ± 0.85 per cent over an approximately seven month period when $R_h = -3.4$ to -2 au. It is possible that seasonal variations can account for some of this difference since the dates of our appulses do not overlap with the dates of the Bieler et al. (2015) measurements. However, Bieler et al. (2015) find no evidence of systematically increasing O_2/H_2O in their measurements, almost all of which have $O_2/H_2O < 0.1$, and several of the best-fitting values in Table 4 have $O_2/H_2O > 0.5$.

2.1 Adopted Values of N_{H_2O} and O_2/H_2O

We tested our fitting procedure by forward modelling simulated data with pre-defined, 'true', values of S/N, N_{H_2O} and O_2/H_2O. We began with a flat-spectrum source ($F(\lambda) = 1$ at all wavelengths) upon which we superimposed H_2O absorption with a column density uniformly drawn from the range $15 < \log N_{H_2O} < 17.5$, O_2, CO and CO_2 absorption with a column density relative to water uniformly drawn from the range 0–100 per cent, and CH_4, C_2H_2, C_2H_6, C_2H_4, C_4H_2 and H_2CO absorption with a column density relative to H_2O uniformly drawn from the range 0–1 per cent. These are the same ranges that were used in the fits to the appulse observations.

Next, we added to the spectrum Poisson noise that had a median S/N in the 1250–2000 Å range chosen uniformly from $0.7 < \log S/N < 2.3$, bracketing the observed values. A template for the S/N as a function of wavelength was derived from the revisit (i.e. unocculted) spectra of our appulse targets by normalizing each spectrum to have the same median S/N from 1250–2000 Å. Then at each wavelength we chose the median 'normalized S/N' value from all of the spectra to form the S/N profile of a 'typical' appulse star. This template achieves peak S/N at ∼1350Å and varies by a factor of ∼10 over the wavelength range 950–2000 Å.

This noisy, simulated spectrum was then treated just like the stellar appulse observations; i.e. it was normalized to have $\langle F(\lambda)\rangle = 1$ from 1800–1900 Å and then fit with the same procedure described above. The best-fitting column densities and uncertainties were then saved along with the true values used to generate the simulated spectrum, and the process was repeated 500 000 times to thoroughly sample the full range of parameter space.

The best-fitting and true values of N_{H_2O} and O_2/H_2O are compared as a function of S/N in Fig. 4. These images are two-dimensional histograms, where the colour bars display the mean offset between the best-fitting and true values in a given bin. Systematic offsets are present in both N_{H_2O} and O_2/H_2O when S/N < 10, but are quite modest at the higher S/N values typical of our appulse observations (see Table 4). Fig. 5 is similar to Fig. 4, except its colour bars display the RMS deviations between the best-fitting and true values in a given bin after correcting for the systematic offsets in Fig. 4. These deviations quantify the spread in true values that are associated with a particular best-fitting value.

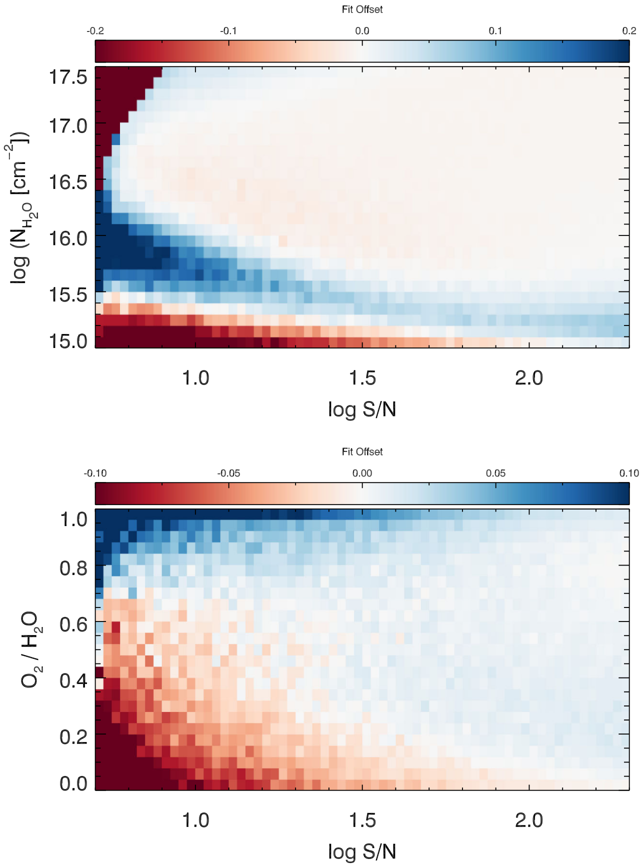

Figure 4. Average offsets between the true and best-fitting values of $\log N_{H_2O}$ (top) and O_2/H_2O (bottom) as a function of log S/N. When S/N > 10, the magnitude of the $\log N_{H_2O}$ offset is typically $\lesssim$0.05 dex, and the magnitude of the O_2/H_2O offset is $\lesssim$0.02.

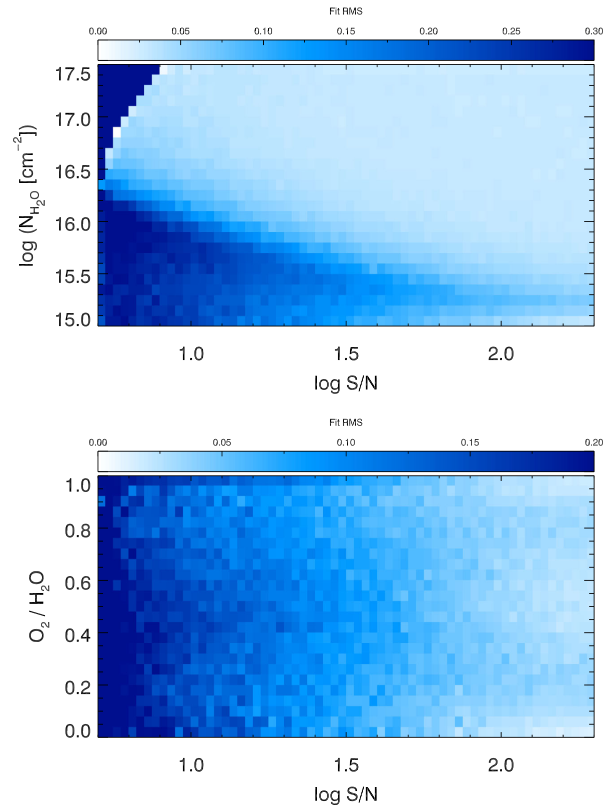

Figure 5. RMS deviations between the true and best-fitting values of $\log N_{H_2O}$ (top) and O_2/H_2O (bottom) as a function of log S/N, after correcting for the systematic offsets in Fig. 4. When S/N > 10, the RMS of $\log N_{H_2O}$ is typically 0.05–0.10 dex and the RMS of O_2/H_2O is ~0.05.

The 'adopted' values of N_{H_2O} and O_2/H_2O are derived from our Monte Carlo simulations by identifying the 1000 simulated spectra with S/N and best-fitting values closest to those measured for a given observation, and fitting a Gaussian to the distribution of true values. We treat the mean of this Gaussian as the adopted value and its standard deviation as the 1σ uncertainty. Since our fits constrain the allowable range of O_2/H_2O, we quote limits whenever the adopted value is $<3\sigma$ from these boundaries.

The last two columns of Table 4 list the adopted values of $\log N_{H_2O}$ and O_2/H_2O, respectively, for our stellar appulse observations. Fig. 6 shows absorption profiles of H_2O and O_2 and their associated 95 per cent (2σ) confidence bands using the adopted values for the appulse of HD 26912. These profiles are overlaid on the normalized stellar spectrum as in Fig. 3, along with confidence bands for the sum of all other modelled species and the total absorption from all species. These profiles clearly show that the adopted values of $\log N_{H_2O}$ and O_2/H_2O are consistent with the data. Absorption profiles derived from the adopted values for all targeted and serendipitous appulses are presented in Appendix B.

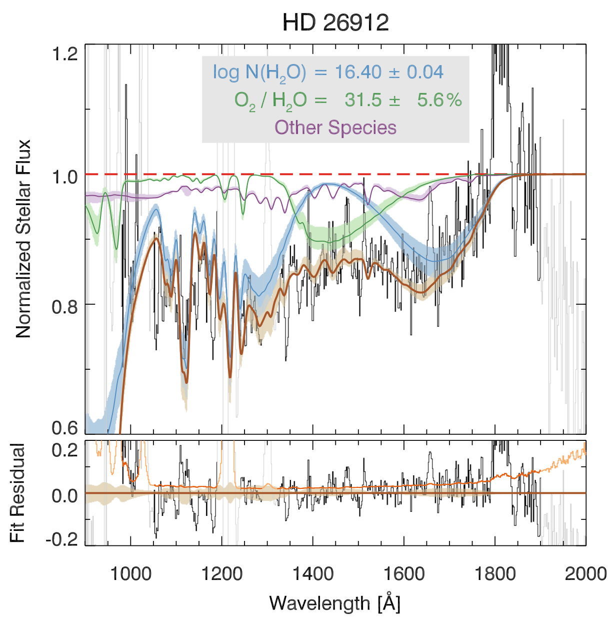

Figure 6. Adopted column densities for the appulse of HD 26912 (FQ = 2), with 95 per cent (2σ) confidence bands. Top: the normalized stellar flux with ensemble fit (brown) and individual-species absorption overlaid using the adopted column densities of H_2O and O_2 from Table 4. Bottom: the residual of the ensemble fit with 1σ flux uncertainty (orange) overlaid. Masked regions are shown in lighter hues in both panels; these regions are not used to constrain the fits. Adopted column densities for all targeted and archival stellar appulses are shown in Appendix B.

3 DISCUSSION

3.1 H_2O Column Densities

The Monte Carlo simulations presented in Section 2.1 are one way to gain confidence in the validity of our absorption fits. Another is to compare our H_2O column densities with values measured by

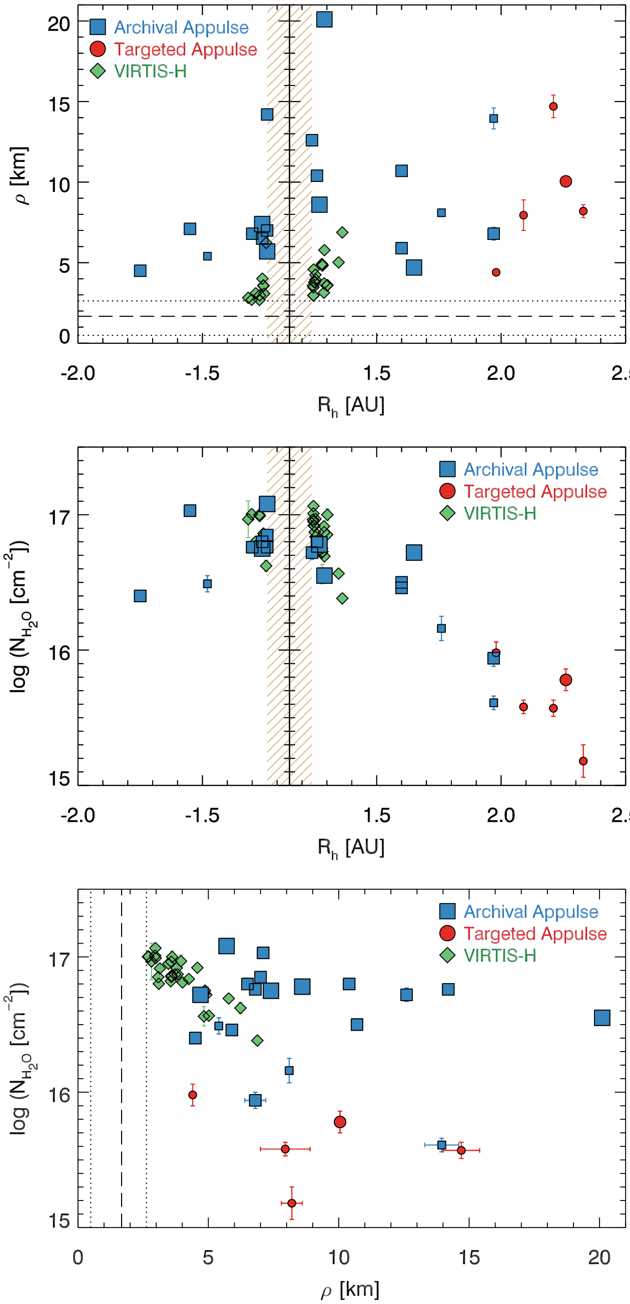

Figure 7. Top: distribution of the stellar appulse observations with heliocentric radius (R_h) and impact parameter (ρ). Middle: distribution of the adopted values of N_{H_2O} with R_h. Bottom: distribution of the adopted values of N_{H_2O} with ρ. The VIRTIS-H measurements of Bockelée-Morvan et al. (2016) are also plotted in all three panels. Heliocentric distances in the beige hatched region are smaller than the perihelion distance of 1.24 au. The dashed line in the top and bottom panels is the effective radius of the nucleus, and the dotted lines indicate its minimum and maximum radii. Symbol size encodes fit quality in all panels, with higher quality fits (lower FQ values) having larger symbols; points with no error bars have uncertainties smaller than the symbol size.

other instruments on *Rosetta* at similar times. Fig. 7 shows the adopted values of $\log N_{H_2O}$ for our stellar appulse observations as a function of R_h, compared to the VIRTIS-H measurements of Bockelée-Morvan et al. (2016). Despite the large scatter in the column densities for a given value of R_h, the adopted values for our appulse observations are reassuringly similar to the measured values from VIRTIS. One reason for the differences that do exist is the fact that the VIRTIS measurements were taken at systematically lower impact parameters than the appulses, as shown in the top panel of Fig. 7.

While the N_{H_2O} values from Alice and VIRTIS are in good agreement, there may be discrepancies with the ROSINA measurements. Fougere et al. (2016) present a sophisticated Direct Simulation Monte Carlo (DSMC) model of the major species (H_2O, CO_2, CO and O_2) in the coma of 67P/C–G, which derives molecular production rates from a non-uniform surface activity distribution. The DSMC model does a remarkable job of reproducing the *in situ* ROSINA measurements of the number density of these species for all data taken before 2016 March (Fougere et al. 2016). However, when the model production rates are used to predict the N_{H_2O} values along the lines of sight probed by Bockelée-Morvan et al. (2016), it finds model column densities that are four times higher than those measured by VIRTIS (Fougere et al. 2016). The cause of this discrepancy is unclear, which illustrates the difficulty of directly comparing measurements from *in situ* instruments such as ROSINA to those from remote-sensing instruments such as VIRTIS and Alice.

3.2 O_2/H_2O

Fig. 8 shows the relative abundance of O_2 with respect to H_2O (top panel) and the column density of O_2 (bottom panel) as a function of R_h. Fig. 9 shows the same quantities as a function of impact parameter. The relative O_2/H_2O abundance tends to increase with increasing heliocentric distance and increasing impact parameter. These correlations (3.9σ and 2.5σ significance, respectively, according to Kendall's tau test) cause the distributions of N_{O_2} as a function of R_h and ρ to be flatter than the corresponding distributions of N_{H_2O} shown in Fig. 7.

The relatively flat distribution of N_{O_2} as a function of ρ is particularly interesting, as it suggests a distributed source of O_2. This would seem to argue against the variety of mechanisms that Mousis et al. (2016) suggest for trapping O_2 in the icy H_2O matrix of 67P/C–G. Formation of O_2 through the dismutation of H_2O_2 during the evaporation of H_2O ice, as suggested by Dulieu et al. (2017), might be able to explain the shape of the O_2/H_2O distribution as a function of ρ. Interestingly, ROSINA detects H_2O_2 in the coma of 67P/C–G (see Fig. 4 of Le Roy et al. 2015 and Fig. 4 of Bieler et al. 2015), but with a relative abundance of $H_2O_2/O_2 < 0.1$ per cent (Bieler et al. 2015), far less than the ratio of $H_2O_2/O_2 = 2$ predicted by the dismutation reaction (Dulieu et al. 2017).

Feldman et al. (2016) used Alice to study gaseous outbursts in the coma of 67P/C–G. These outbursts exhibit no increase in long-wavelength solar reflected light that would indicate an increase in dust production, and are characterized by a sudden increase in the brightness ratio of O I $\lambda1356/\lambda1304$ in the sunward coma. Feldman et al. (2016) infer that these outbursts are driven by O_2 release, and estimate that $O_2/H_2O \geq 50$ per cent during the outbursts.

Coincidentally, our earliest archival appulse (HD 26912; see Fig. 3 and Fig. 6) occurred during the onset of one of the Feldman et al. (2016) outbursts (see their section 2.5). We adopt $O_2/H_2O = 31.5 \pm 5.6$ per cent for this appulse (see Table 4), which is somewhat lower than the Feldman et al. (2016) estimate. This apparent discrepancy is likely a result of timing differences; i.e. the adopted value from the appulse measures the ambient O_2/H_2O in the coma just prior to outburst, whereas the Feldman et al. (2016)

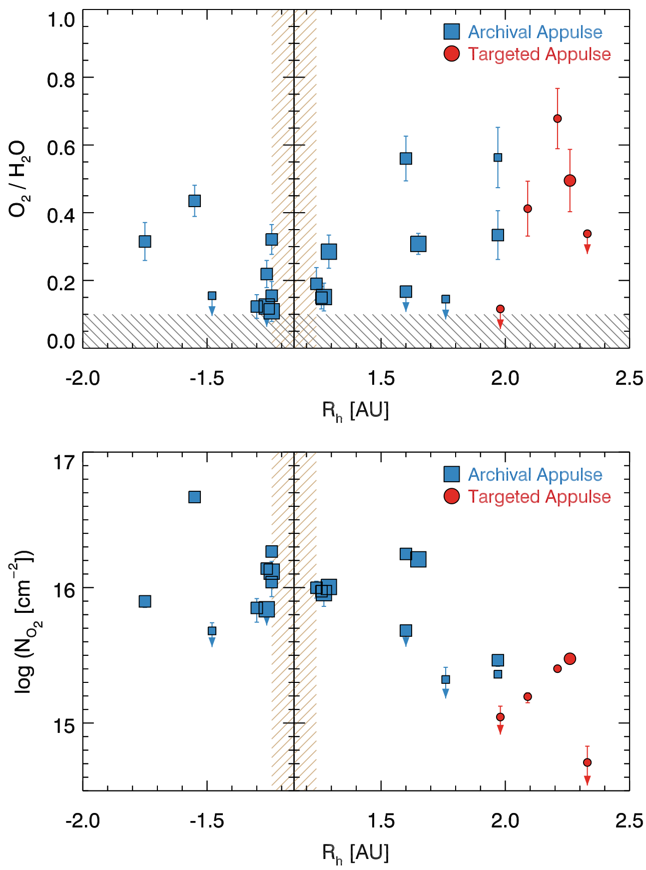

Figure 8. O_2/H_2O (top) and N_{O_2} (bottom) as a function of R_h. Symbol sizes are the same as in Fig. 7. Heliocentric distances in the beige hatched region are smaller than the perihelion distance of 1.24 au. The grey hatched region in the top panel indicates typical values of O_2/H_2O measured by ROSINA (Bieler et al. 2015; Fougere et al. 2016).

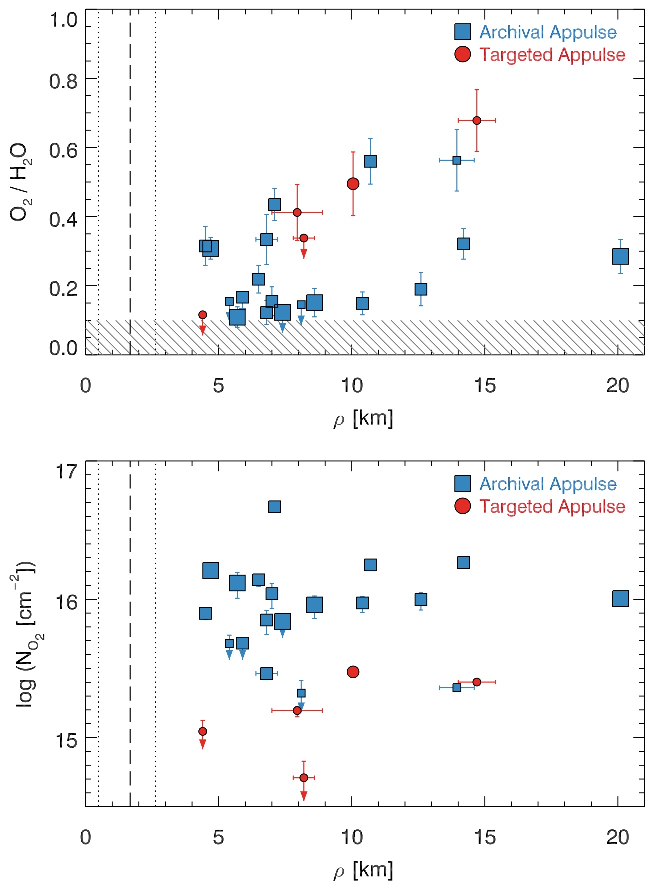

Figure 9. O_2/H_2O (top) and N_{O_2} (bottom) as a function of impact parameter. Symbol sizes are the same as in Fig. 7. The dashed vertical line is the effective radius of the nucleus and the dotted vertical lines indicate its minimum and maximum radii.

value measures the peak O_2/H_2O over the ∼30-minute duration of the outburst.

As mentioned in Section 2, the O_2/H_2O values in Table 4 are generally higher, and have considerably larger scatter, than the values found by ROSINA–DFMS. Bieler et al. (2015) found $n_{O_2}/n_{H_2O} = 3.85 \pm 0.85$ per cent in data taken between 2014 August and 2015 March, and Fougere et al. (2016) found $Q_{O_2}/Q_{H_2O} \approx 2$ per cent throughout the time frame of our appulse observations. Notably, neither Bieler et al. (2015) nor Fougere et al. (2016) list a single observation where $O_2/H_2O > 15$ per cent, but we find a median value of 25 per cent.

As discussed in Section 3.1, comparisons between the *in situ* measurements of ROSINA and the line-of-sight measurements of Alice and VIRTIS are not straightforward, even with a sophisticated coma model (Fougere et al. 2016). None the less, the large values of O_2/H_2O derived from the Alice data are surprising. While we have included several minor species in our absorption fits (see Section 2), there are many species detected in the coma of 67P/C–G by ROSINA for which we were unable to find absorption cross-sections (e.g. HS, S_2, CH_4O; Le Roy et al. 2015). Some of these 'missing' species could have cross-sections large enough to cause measurable far-UV absorption, even for very small column densities, causing the current O_2/H_2O values to be over-estimated. Quantifying the magnitude of these systematic uncertainties is exceedingly difficult without additional laboratory data for far-UV molecular absorption cross-sections.

Further, even if our fits currently include all of the relevant species, the absorption cross-sections we use were all measured at $T \approx 300$ K (see Table 3). Since the absorbing coma gas is expected to be at lower temperature, variations in the absorption cross-sections with temperature could lead us to infer incorrect values of the column density with our current procedure. However, the scant existing data suggest that our procedure under-estimates the amount of low-temperature O_2 present by assuming room-temperature cross-sections (see discussion in Section 2; Yoshino et al. 2005), which would serve to increase the discrepancy between our results and those of ROSINA.

4 CONCLUSIONS

Using the Alice far-UV imaging spectrograph aboard *Rosetta*, we have independently verified the presence of O_2 in the coma of Comet 67P/C–G. O_2 was detected for the first time in the coma of a comet by *Rosetta*'s ROSINA mass spectrometer (Bieler et al. 2015; Fougere et al. 2016). In the present study, both O_2 and H_2O were detected in far-UV absorption against the continuum of stars located near the nucleus of 67P/C–G, at impact parameters of 4–20 km. These stellar appulses occurred at heliocentric distances of −1.8 to 2.3 au, where negative distances indicate pre-perihelion observations. The main results of our analysis are as follows:

(i) the H_2O column densities derived from the stellar spectra are in good agreement with VIRTIS-H measurements from the same time period taken at similar impact parameters (Bockelée-Morvan et al. 2016); and

(ii) the median value for the relative abundance of O_2 with respect to H_2O derived from the stellar spectra is $O_2/H_2O = 25$ per cent. This value is considerably higher than those reported by ROSINA; Bieler et al. (2015) and Fougere et al. (2016) found mean values of $O_2/H_2O < 5$ per cent.

We see no simple explanation for the difference in O_2/H_2O measured by Alice and ROSINA, unless it is related to the unmodelled species and $T = 300$ K cross-sections discussed at the end of Section 3.2. The Alice H_2O measurements are consistent with the values published by other remote-sensing instruments on *Rosetta*; and while this does not guarantee that our O_2 values are correct, it does suggest that our measurements are reasonably robust. The ROSINA measurements, on the other hand, are performed *in situ* at the spacecraft location, and the sophisticated coma model of Fougere et al. (2016) is designed to reproduce these measurements. This same model has difficulty reproducing the H_2O column densities of Bockelée-Morvan et al. (2016), which were measured very close to perihelion (Fougere et al. 2016). There is clearly much future work to be done to reconcile these differences.

ACKNOWLEDGEMENTS

Rosetta is an ESA mission with contributions from its member states and NASA. We thank the members of the *Rosetta* Science Ground System and Mission Operations Center teams, in particular Richard Moissl and Michael Küppers, for their expert and dedicated help in planning and executing the Alice observations. The Alice team acknowledges continuing support from NASA via Jet Propulsion Laboratory contract 1336850 to the Southwest Research Institute. This research has made use of the SIMBAD data base, operated at CDS, Strasbourg, France.

REFERENCES

Ackerman M., Biaume F., Kockarts G., 1970, Planet. Space Sci., 18, 1639
Acton C. H., 1996, Planet. Space Sci., 44, 65
Balsiger H. et al., 2007, Space Sci. Rev., 128, 745
Barucci M. A. et al., 2016, A&A, 595, A102
Bieler A. et al., 2015, Nature, 526, 678
Bockelée-Morvan D. et al., 2016, MNRAS, 462, S170
Brion C. E., Tan K. H., 1979, J. Electron. Spectrosc. Relat. Phenom., 17, 101
Cairns R. B., Samson J. A. R., 1965, J. Geophys. Res., 70, 99
Chan W. F., Cooper G., Brion C. E., 1993, Chem. Phys., 178, 401
Chung C.-Y., Chew E. P., Cheng B.-M., Bahou M., Lee Y.-P., 2001, Nuclear Instrum. Methods Phys. Res. A, 467, 1572
Coradini A. et al., 2007, Space Sci. Rev., 128, 529
Ditchburn R. W., 1955, Proc. R. Soc., 229, 44
Dulieu F., Minissale M., Bockelée-Morvan D., 2017, A&A, 597, A56
Fahr A., Nayak A. K., 1994, Chem. Phys., 189, 725
Feldman P. D. et al., 2015, A&A, 583, A8
Feldman P. D. et al., 2016, ApJ, 825, L8
Fougere N. et al., 2016, MNRAS, 462, S156
Gentieu E. P., Mentall J. E., 1970, Science, 169, 681
Gulkis S. et al., 2007, Space Sci. Rev., 128, 561
Hitchcock A. P., Brion C. E., van der Wiel M. J., 1980, Chem. Phys., 45, 461
Huebner W. F., Mukherjee J., 2015, Planet. Space Sci., 106, 11
Koch E. E., Skibowski M., 1971, Chem. Phys. Lett., 9, 429
Le Roy L. et al., 2015, A&A, 583, A1
Lee S. et al., 2015, A&A, 583, A5
Lombos B. A., Sauvageau P., Sandorfy C., 1967, J. Mol. Spectrosc., 24, 253
Markwardt C. B., 2009, in Bohlender D. A., Durand D., Dowler P., eds, ASP Conf. Ser. Vol. 411, Astronomical Data Analysis Software and Systems XVIII. Astron. Soc. Pac., San Francisco, p. 251
Mentall J. E., Gentieu E. P., Kraus M., Neumann D., 1971, J. Chem. Phys., 55, 5471
Metzger P. H., Cook G. R., 1964, J. Chem. Phys., 41, 642
Mota R. et al., 2005, Chem. Phys. Lett., 416, 152
Mount G. H., Moos H. W., 1978, ApJ, 224, L35
Mousis O. et al., 2016, ApJ, 823, L41
Nakayama T., Watanabe K., 1964, J. Chem. Phys., 40, 588
Okabe H., 1981, J. Chem. Phys., 75, 2772
Okabe H., Becker D. A., 1963, J. Chem. Phys., 39, 2549
Rubin M., Altwegg K., van Dishoeck E. F., Schwehm G., 2015, ApJ, 815, L11
Schoen R. I., 1962, J. Chem. Phys., 37, 2032
Stark G., Yoshino K., Smith P. L., Ito K., 2007, J. Quant. Spec. Radiat. Transf., 103, 67
Stern S. A. et al., 2007, Space Sci. Rev., 128, 507
Sun H., Weissler G. L., 1955, J. Chem. Phys., 23, 1160
Taquet V., Furuya K., Walsh C., van Dishoeck E. F., 2016, MNRAS, 462, S99
Watanabe K., Jursa A. S., 1964, J. Chem. Phys., 41, 1650
Watanabe K., Zelikoff M., 1953, J. Opt. Soc. Am., 43, 753
Wenger M. et al., 2000, A&AS, 143, 9
Yoshino K., Esmond J. R., Sun W. H., Parkinson W. H., Ito K., Matsui T., 1996, J. Quant. Spec. Radiat. Transf., 55, 53
Yoshino K., Parkinson W. H., Ito K., Matsui T., 2005, J. Mol. Spectrosc., 229, 238
Zelikoff M., Watanabe K., 1953, J. Opt. Soc. Am., 43, 756

APPENDIX A: BEST-FITTING ABSORPTION PROFILES

Figs A1-A29 present best-fitting absorption profiles for all targeted and archival stellar appulses, arranged chronologically. The top panel of each figure displays the normalized stellar flux, with best-fitting ensemble absorption (solid brown line) overlaid. Absorption from H_2O, O_2, and other species are also shown. The bottom panel of each figure displays the residual of the ensemble fit and the 1σ uncertainty of the normalized spectrum.

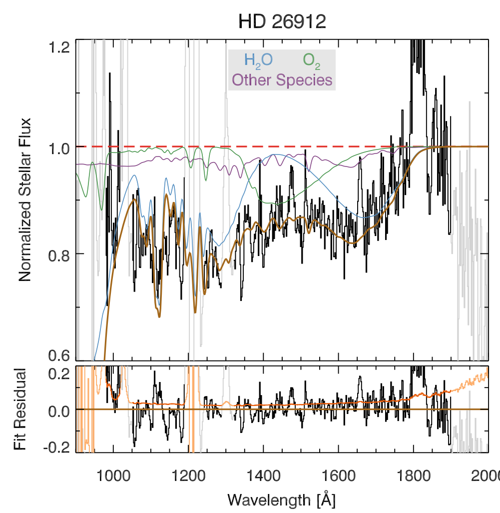

Figure A1. Fits to the appulse absorption of HD 26912 (FQ = 2).

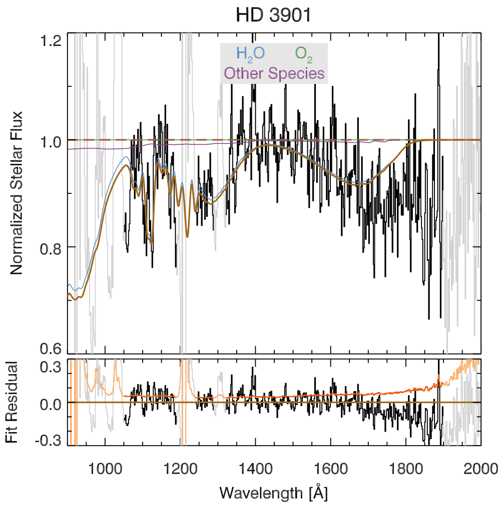

Figure A2. Fits to the appulse absorption of HD 3901 (FQ = 4).

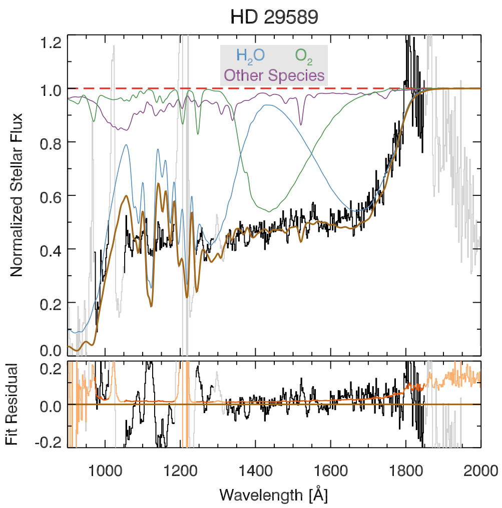

Figure A3. Fits to the appulse absorption of HD 29589 (FQ = 2).

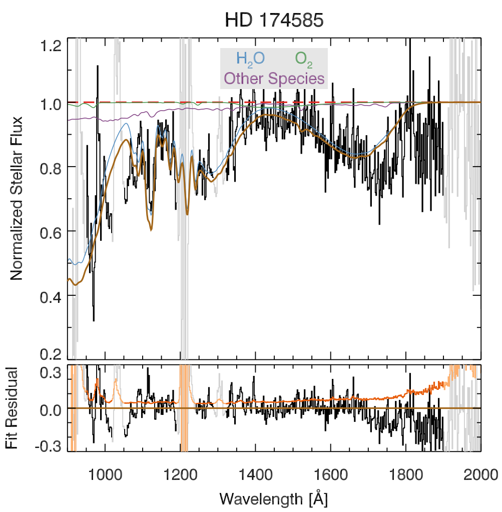

Figure A4. Fits to the appulse absorption of HD 174585 (FQ = 3).

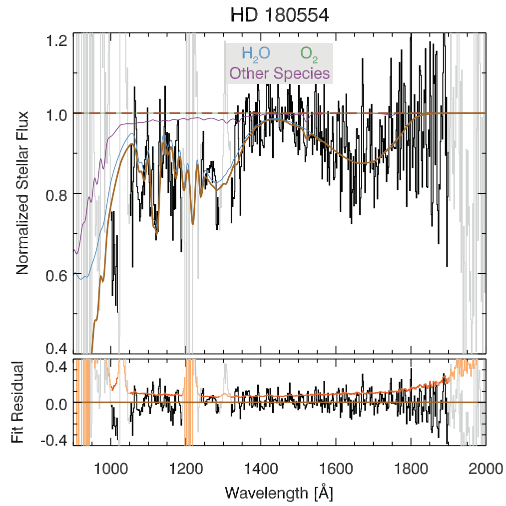

Figure A5. Fits to the appulse absorption of HD 180554 (FQ = 4).

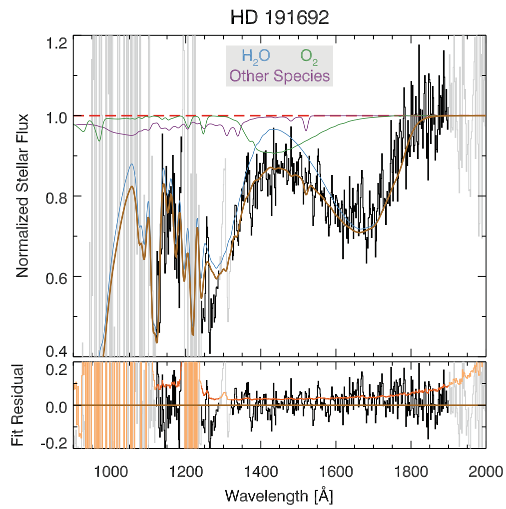

Figure A6. Fits to the appulse absorption of HD 191692 (FQ = 2).

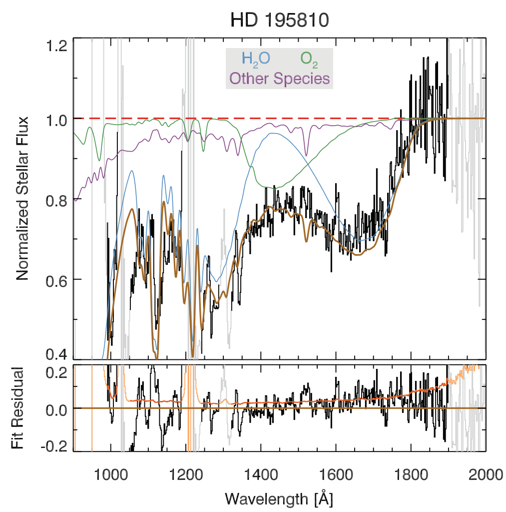

Figure A7. Fits to the appulse absorption of HD 195810 (FQ = 2).

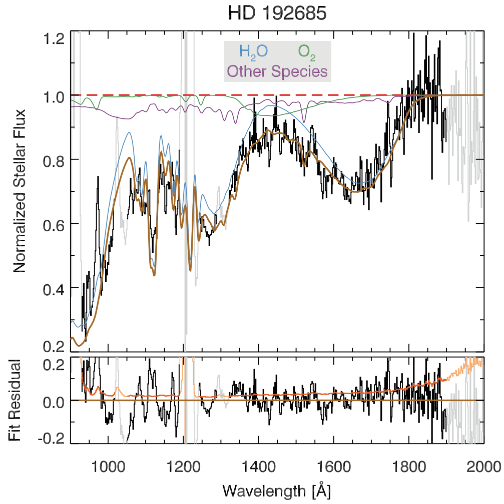

Figure A8. Fits to the appulse absorption of HD 192685 (FQ = 1).

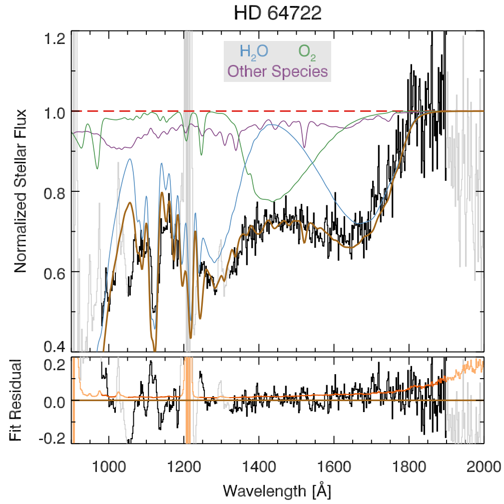

Figure A11. Fits to the appulse absorption of HD 64722 (FQ = 2).

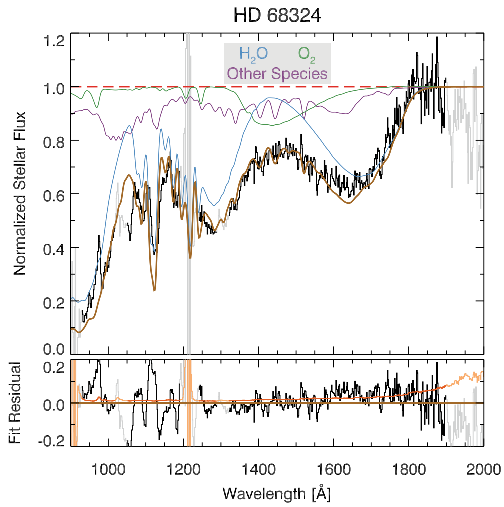

Figure A9. Fits to the appulse absorption of HD 68324 (FQ = 2).

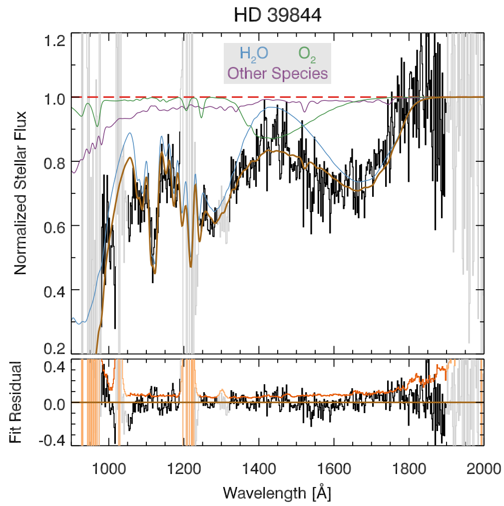

Figure A12. Fits to the appulse absorption of HD 39844 (FQ = 2).

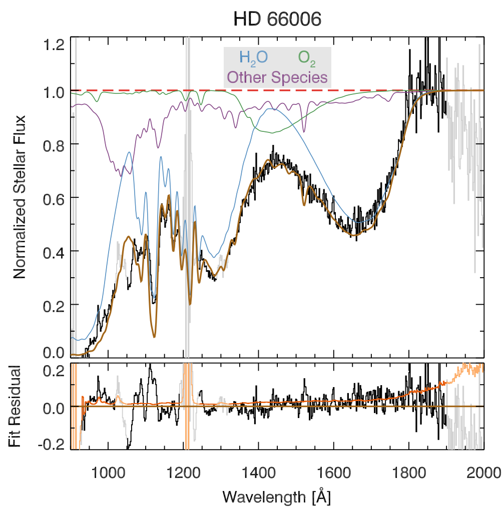

Figure A10. Fits to the appulse absorption of HD 66006 (FQ = 1).

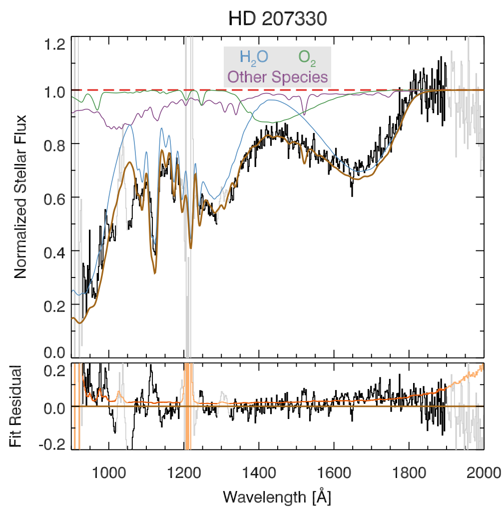

Figure A13. Fits to the appulse absorption of HD 207330 (FQ = 2).

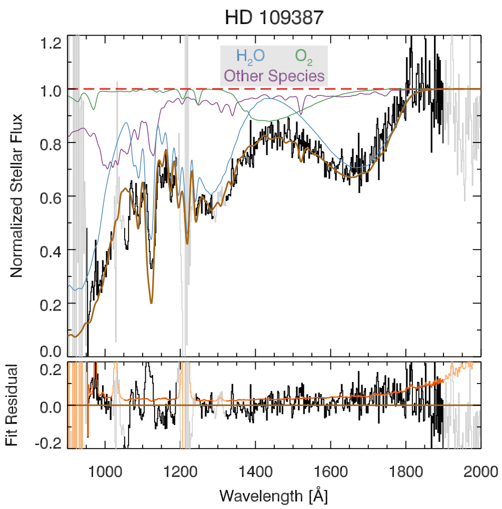

Figure A14. Fits to the appulse absorption of HD 109387 (FQ = 1).

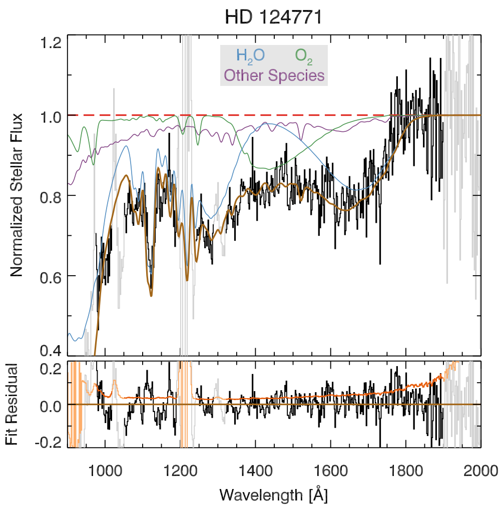

Figure A15. Fits to the appulse absorption of HD 124771 (FQ = 1).

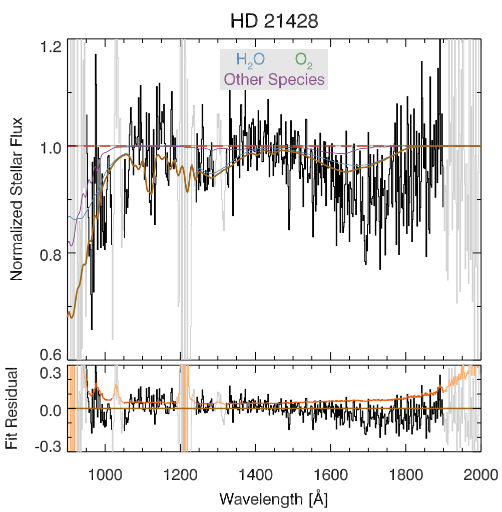

Figure A16. Fits to the appulse absorption of HD 21428 (FQ = 4).

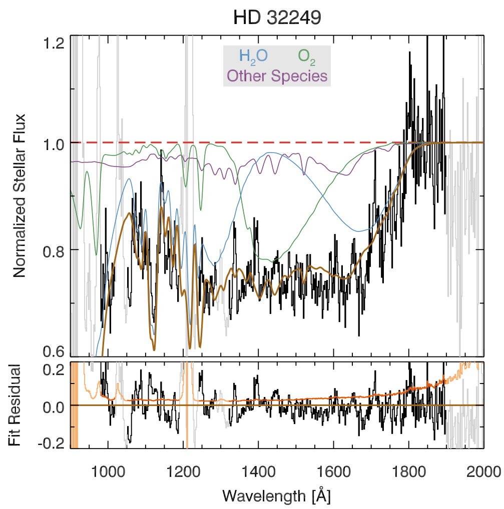

Figure A17. Fits to the appulse absorption of HD 32249 (FQ = 2).

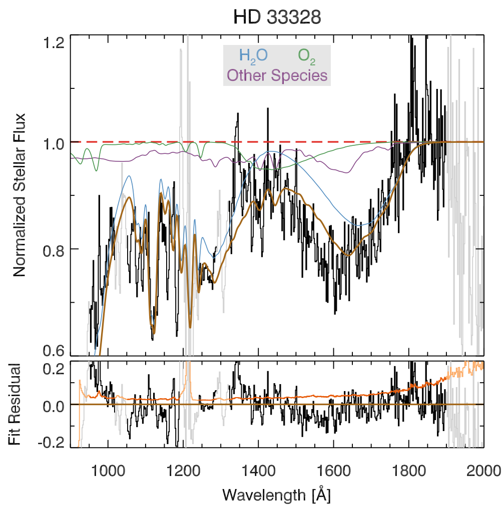

Figure A18. Fits to the appulse absorption of HD 33328 (FQ = 2).

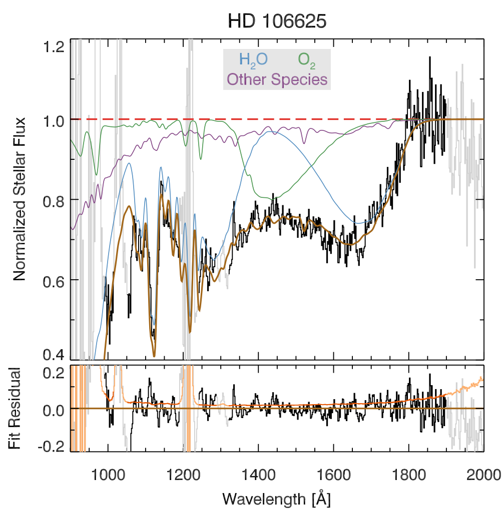

Figure A19. Fits to the appulse absorption of HD 106625 (FQ = 1).

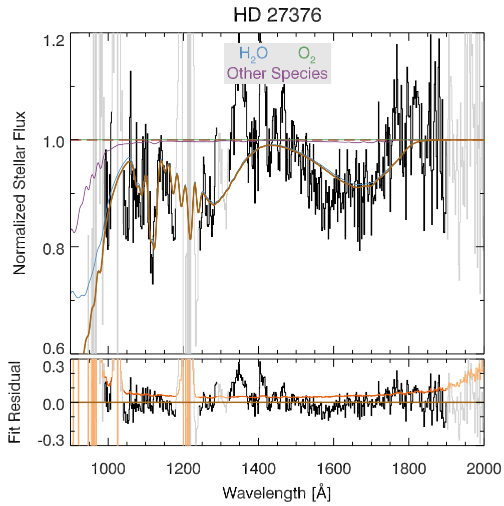

Figure A20. Fits to the appulse absorption of HD 27376 (FQ = 3).

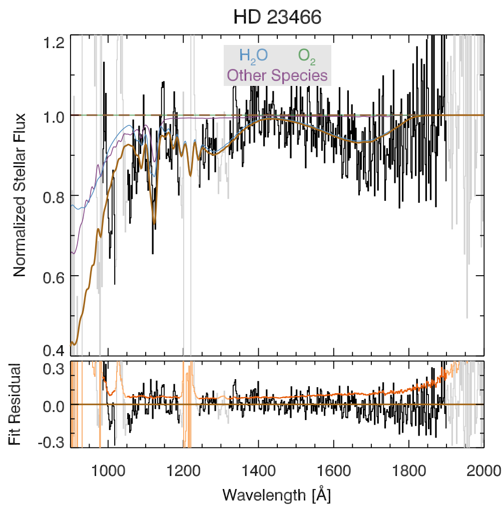

Figure A21. Fits to the appulse absorption of HD 23466 (FQ = 4).

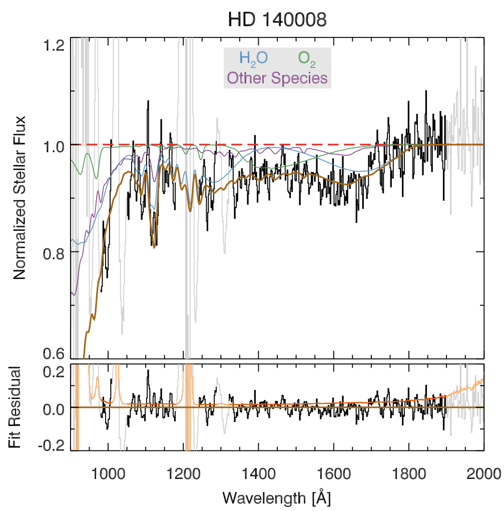

Figure A22. Fits to the appulse absorption of HD 140008 (FQ = 2).

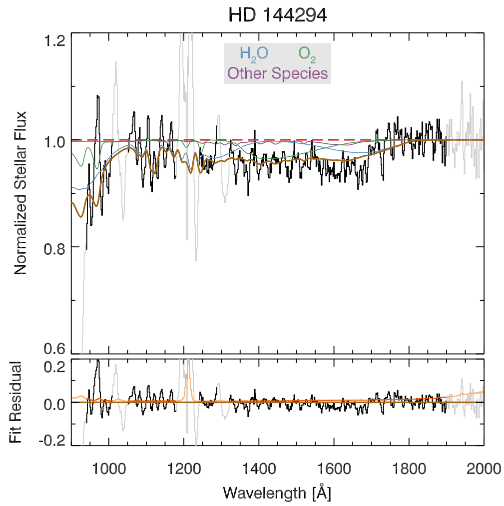

Figure A23. Fits to the appulse absorption of HD 144294 (FQ = 3).

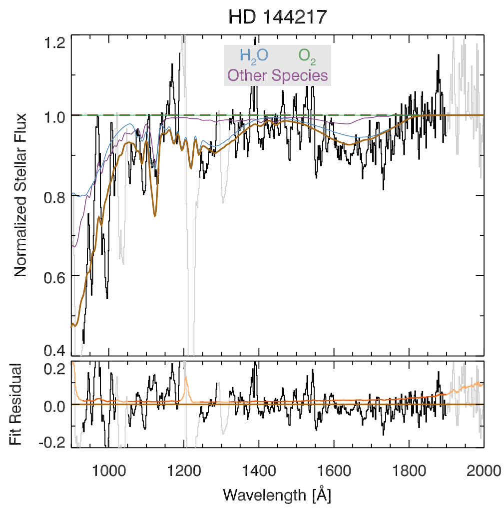

Figure A24. Fits to the appulse absorption of HD 144217 (FQ = 3).

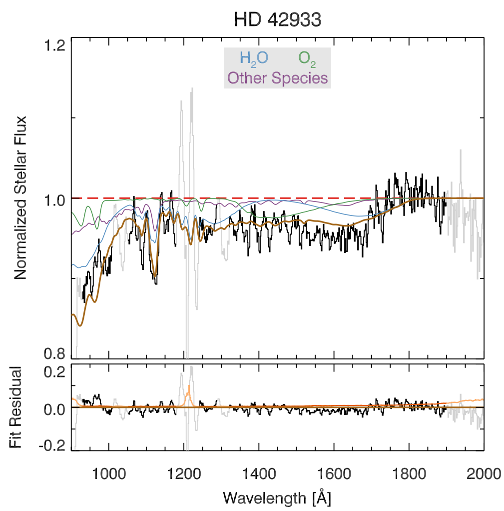

Figure A25. Fits to the appulse absorption of HD 42933 (FQ = 3).

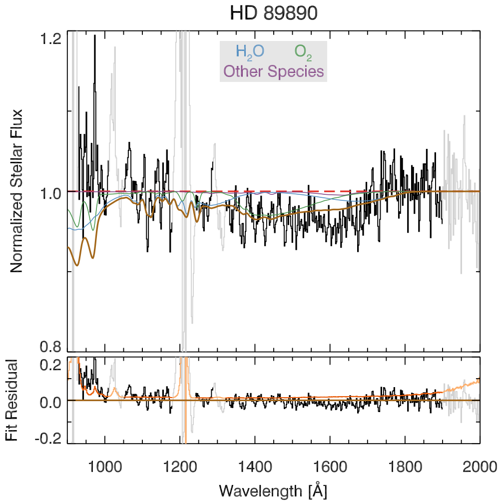

Figure A26. Fits to the appulse absorption of HD 89890 (FQ = 4).

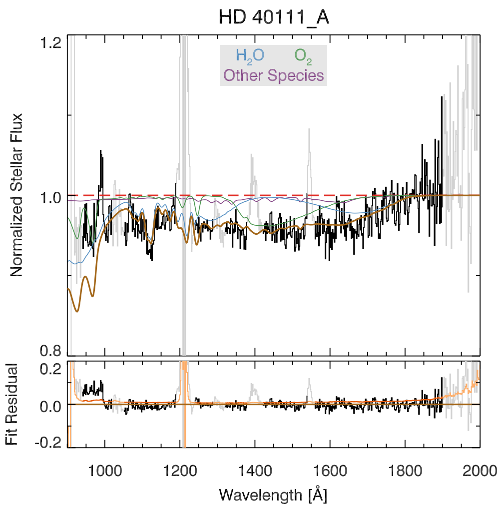

Figure A27. Fits to the first appulse absorption of HD 40111 (FQ = 3).

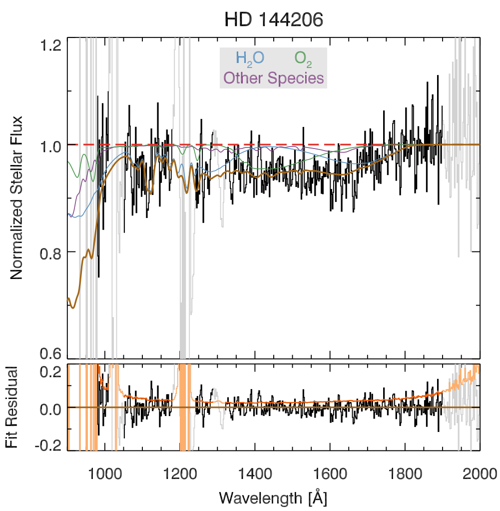

Figure A28. Fits to the appulse absorption of HD 144206 (FQ = 2).

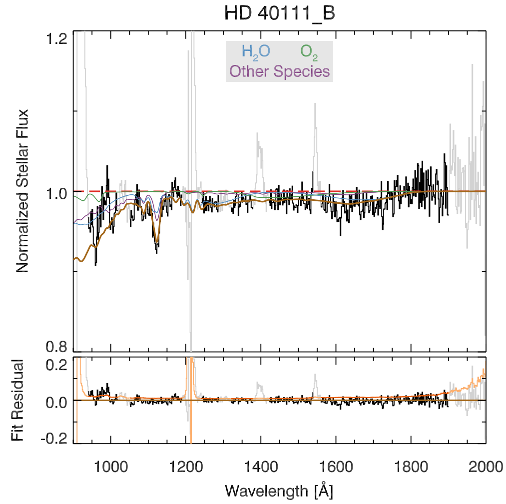

Figure A29. Fits to the second appulse absorption of HD 40111 (FQ = 3).

APPENDIX B: ADOPTED ABSORPTION PROFILES

Figs B1–B29 present the adopted column densities for all targeted and archival stellar appulses, with 95 per cent (2σ) confidence bands. The top panel of each figure displays the normalized stellar flux and associated 95 per cent confidence band (grey), with ensemble fit (brown) and individual-species absorption overlaid using the adopted column densities of H_2O and O_2 from Table 4. The bottom panel of each figure displays the residual of the ensemble fit and the 1σ uncertainty of the normalized spectrum.

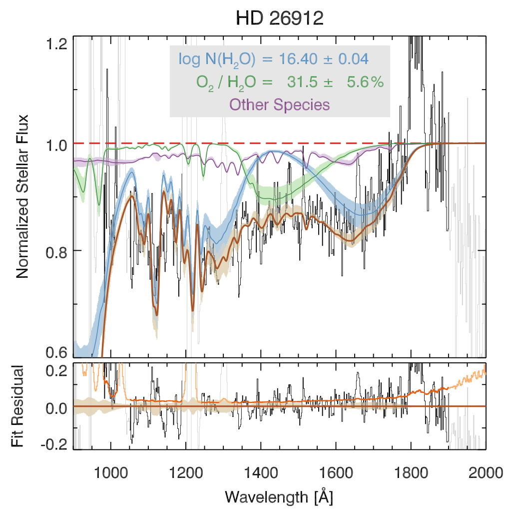

Figure B1. Adopted column densities for the appulse of HD 26912 (FQ = 2), with 95 per cent (2σ) confidence bands.

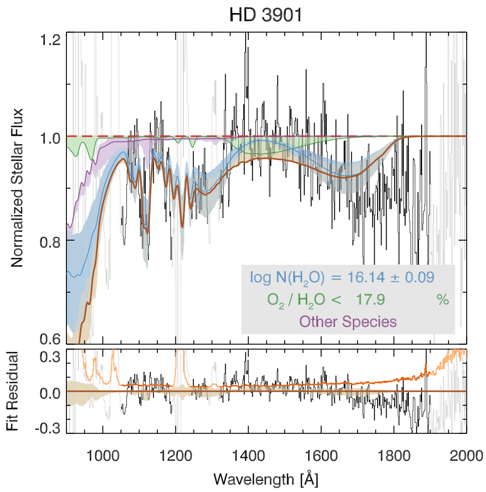

Figure B2. Adopted column densities for the appulse of HD 3901 (FQ = 4), with 95 per cent (2σ) confidence bands.

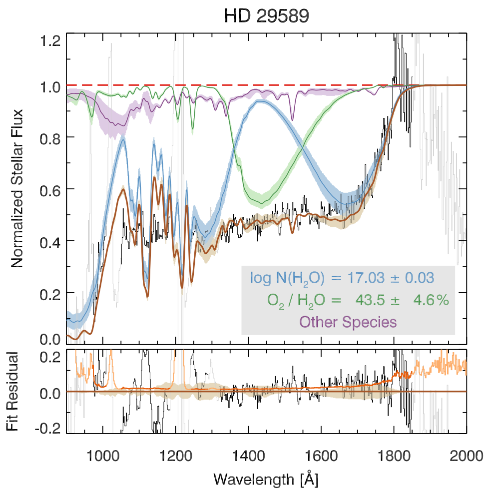

Figure B3. Adopted column densities for the appulse of HD 29589 (FQ = 2), with 95 per cent (2σ) confidence bands.

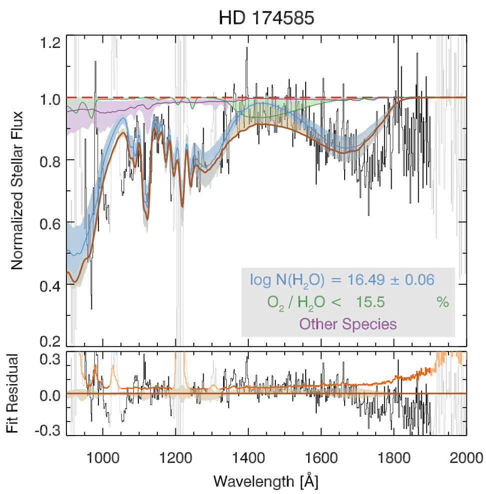

Figure B4. Adopted column densities for the appulse of HD 174585 (FQ = 3), with 95 per cent (2σ) confidence bands.

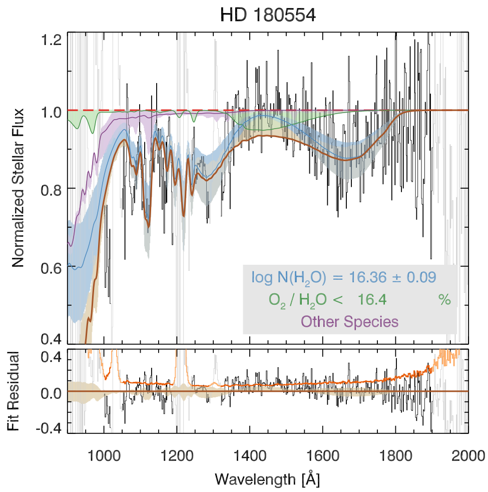

Figure B5. Adopted column densities for the appulse of HD 180554 (FQ = 4), with 95 per cent (2σ) confidence bands.

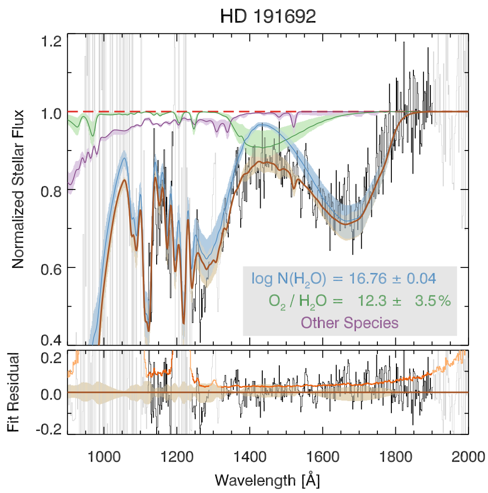

Figure B6. Adopted column densities for the appulse of HD 191692 (FQ = 2), with 95 per cent (2σ) confidence bands.

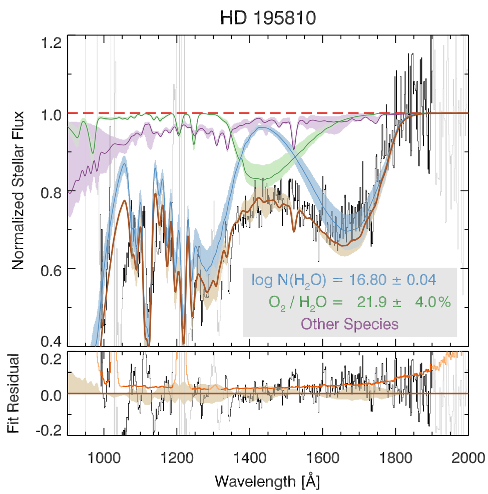

Figure B7. Adopted column densities for the appulse of HD 195810 (FQ = 2), with 95 per cent (2σ) confidence bands.

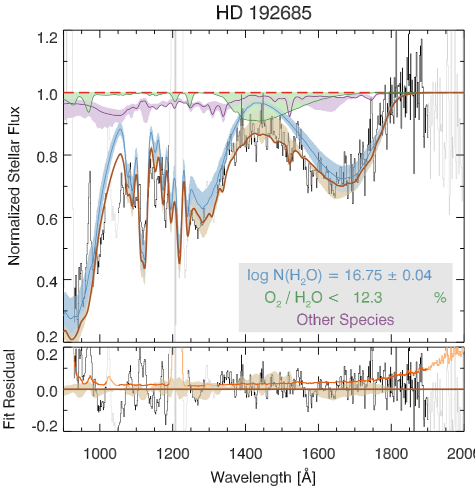

Figure B8. Adopted column densities for the appulse of HD 192685 (FQ = 1), with 95 per cent (2σ) confidence bands.

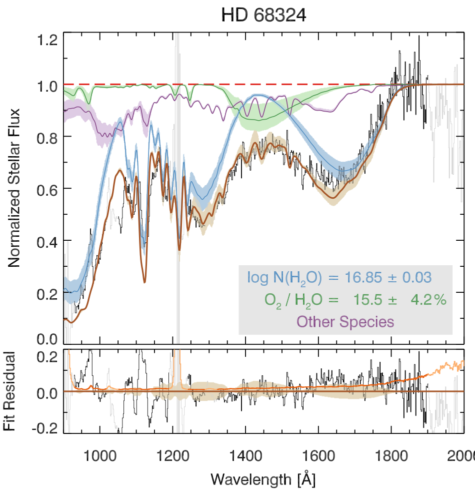

Figure B9. Adopted column densities for the appulse of HD 68324 (FQ = 2), with 95 per cent (2σ) confidence bands.

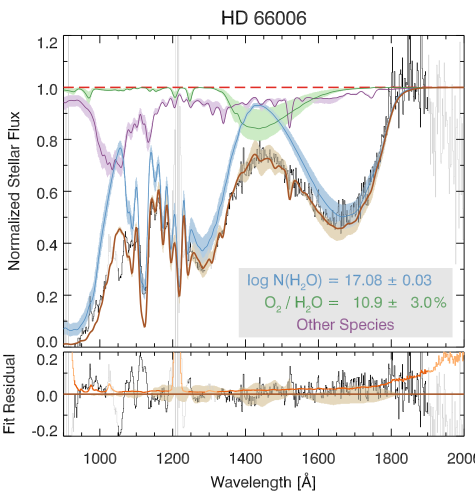

Figure B10. Adopted column densities for the appulse of HD 66006 (FQ = 1), with 95 per cent (2σ) confidence bands.

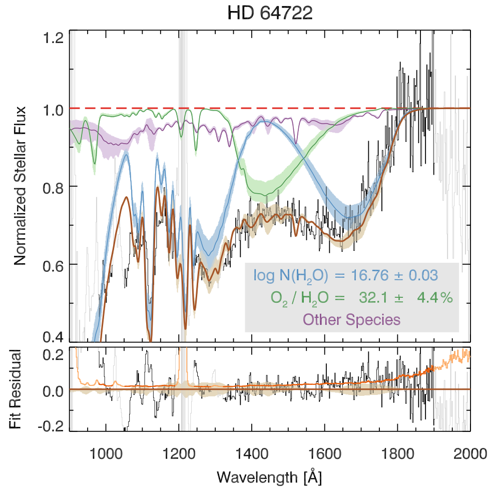

Figure B11. Adopted column densities for the appulse of HD 64722 (FQ = 2), with 95 per cent (2σ) confidence bands.

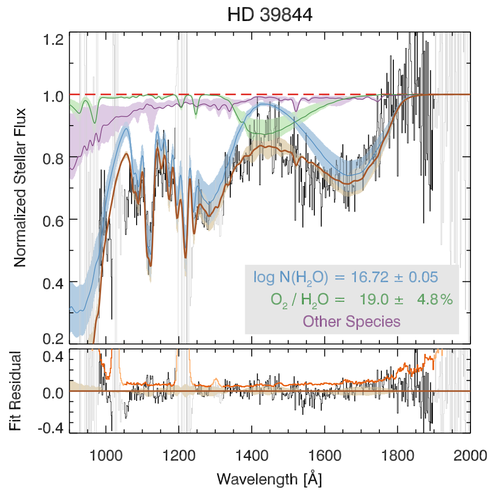

Figure B12. Adopted column densities for the appulse of HD 39844 (FQ = 2), with 95 per cent (2σ) confidence bands.

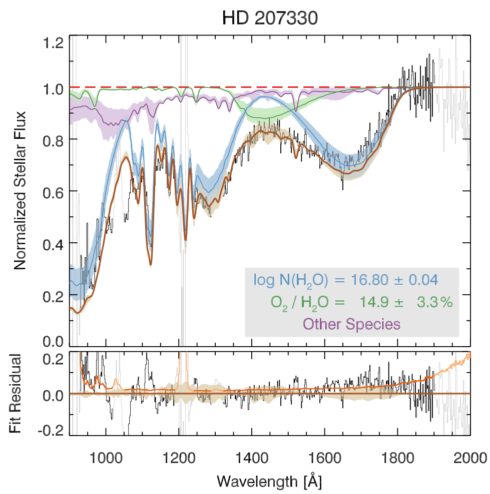

Figure B13. Adopted column densities for the appulse of HD 207330 (FQ = 2), with 95 per cent (2σ) confidence bands.

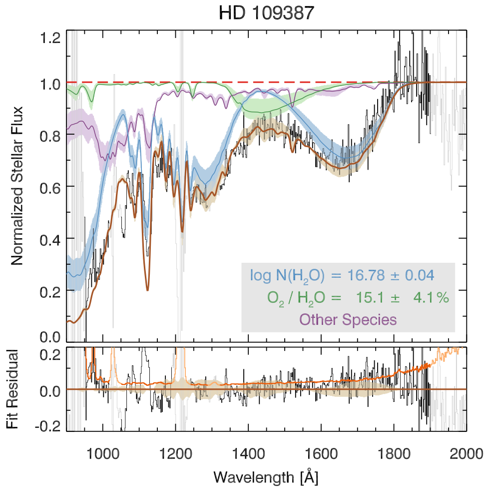

Figure B14. Adopted column densities for the appulse of HD 109387 (FQ = 1), with 95 per cent (2σ) confidence bands.

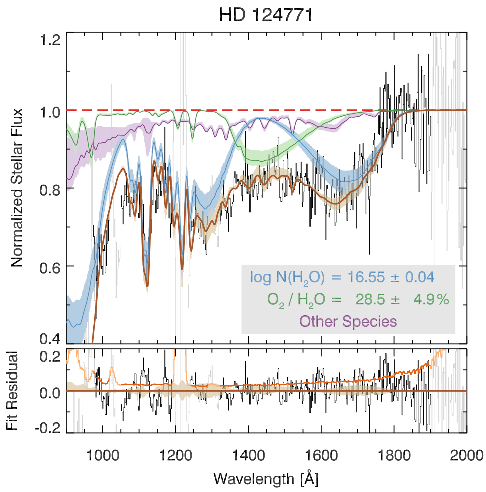

Figure B15. Adopted column densities for the appulse of HD 124771 (FQ = 1), with 95 per cent (2σ) confidence bands.

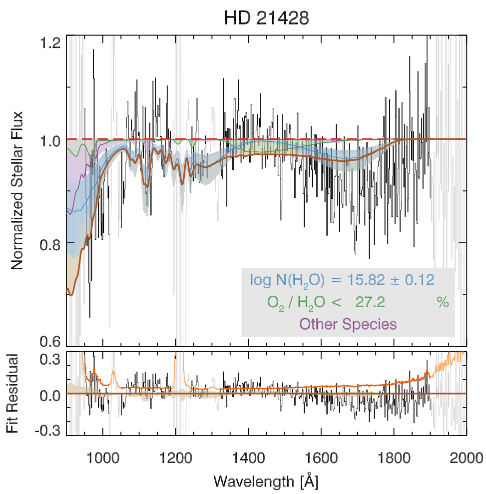

Figure B16. Adopted column densities for the appulse of HD 21428 (FQ = 4), with 95 per cent (2σ) confidence bands.

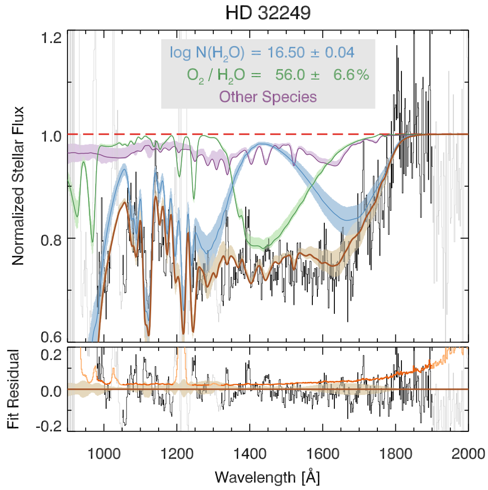

Figure B17. Adopted column densities for the appulse of HD 32249 (FQ = 2), with 95 per cent (2σ) confidence bands.

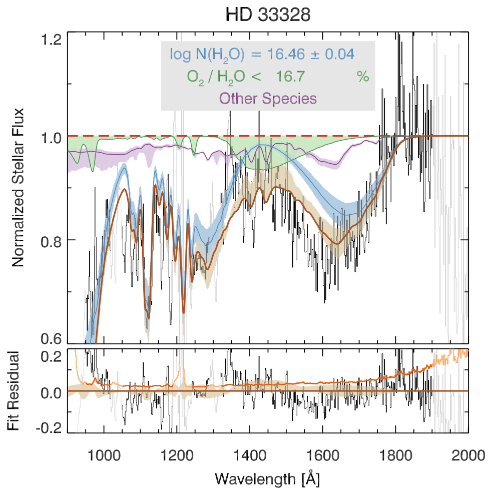

Figure B18. Adopted column densities for the appulse of HD 33328 (FQ = 2), with 95 per cent (2σ) confidence bands.

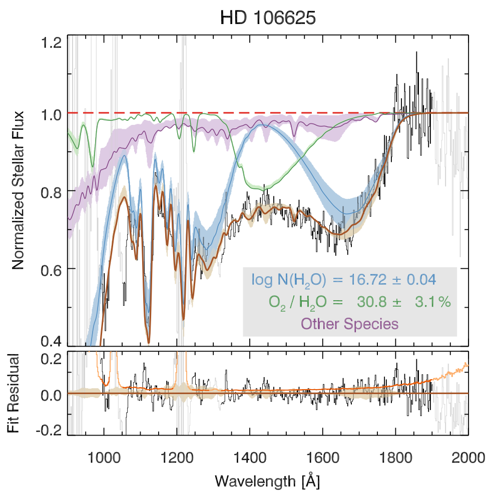

Figure B19. Adopted column densities for the appulse of HD 106625 (FQ = 1), with 95 per cent (2σ) confidence bands.

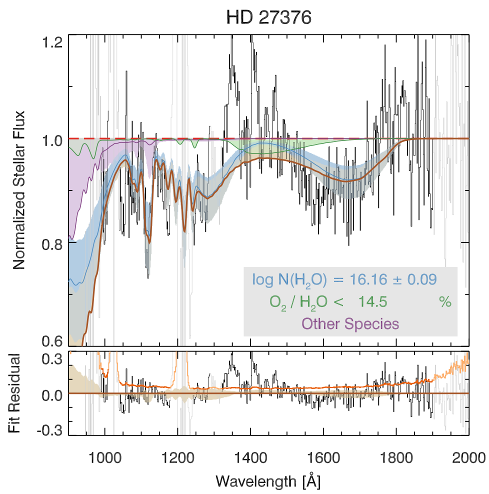

Figure B20. Adopted column densities for the appulse of HD 27376 (FQ = 3), with 95 per cent (2σ) confidence bands.

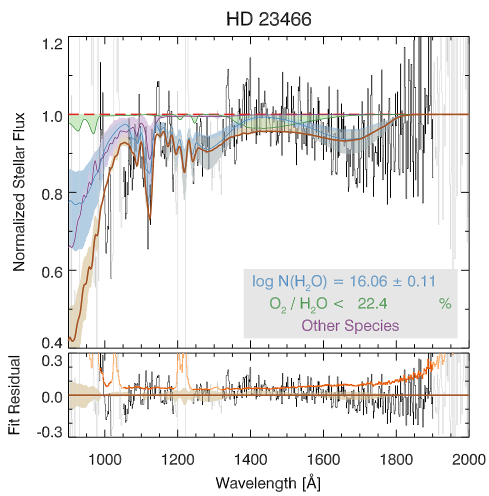

Figure B21. Adopted column densities for the appulse of HD 23466 (FQ = 4), with 95 per cent (2σ) confidence bands.

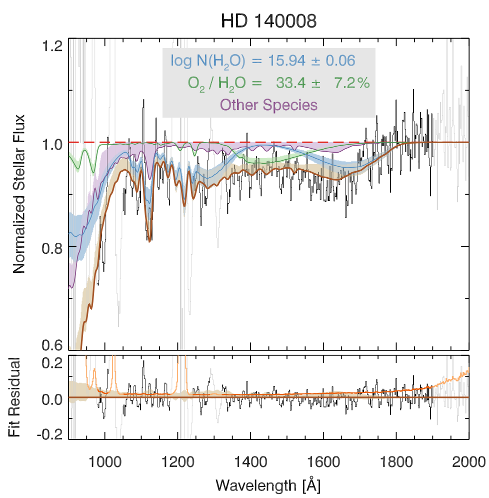

Figure B22. Adopted column densities for the appulse of HD 140008 (FQ = 2), with 95 per cent (2σ) confidence bands.

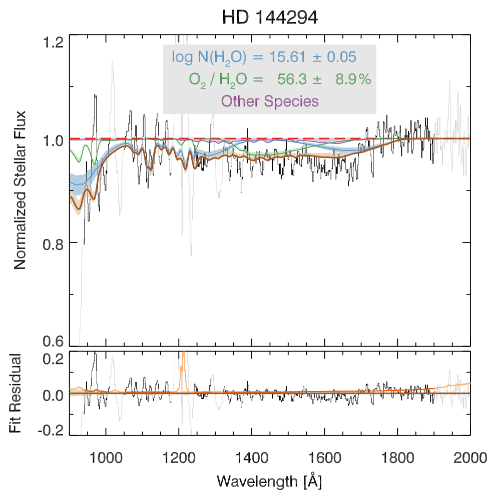

Figure B23. Adopted column densities for the appulse of HD 144294 (FQ = 3), with 95 per cent (2σ) confidence bands.

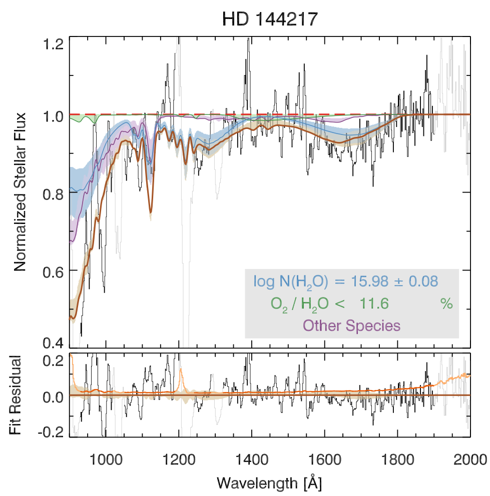

Figure B24. Adopted column densities for the appulse of HD 144217 (FQ = 3), with 95 per cent (2σ) confidence bands.

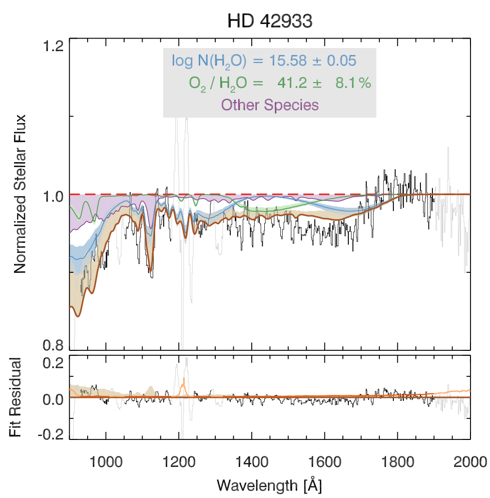

Figure B25. Adopted column densities for the appulse of HD 42933 (FQ = 3), with 95 per cent (2σ) confidence bands.

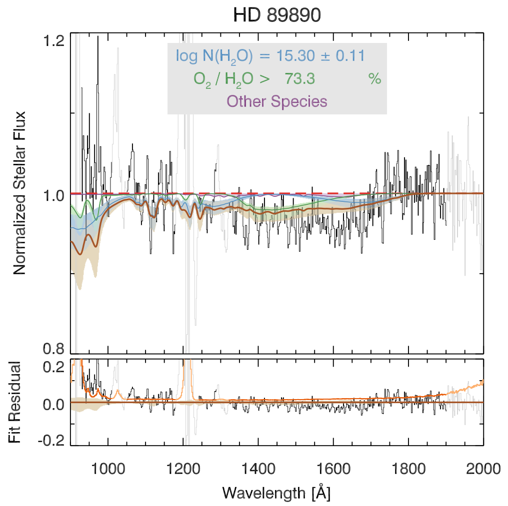

Figure B26. Adopted column densities for the appulse of HD 89890 (FQ = 4), with 95 per cent (2σ) confidence bands.

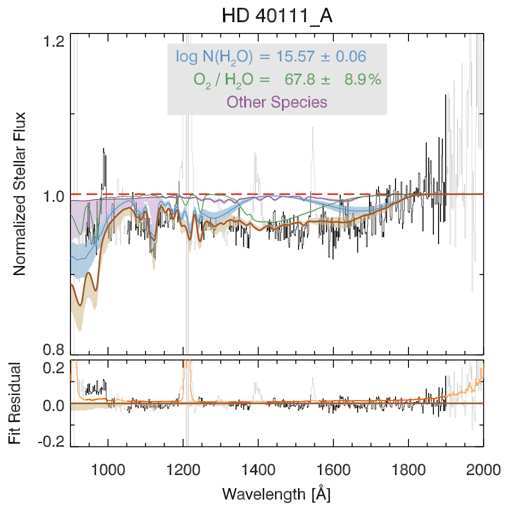

Figure B27. Adopted column densities for the first appulse of HD 40111 (FQ = 3), with 95 per cent (2σ) confidence bands.

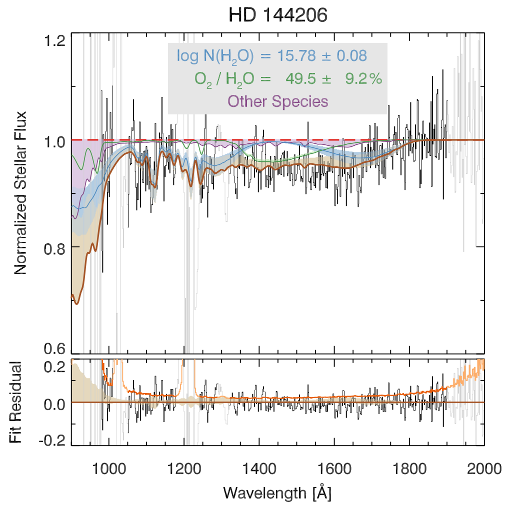

Figure B28. Adopted column densities for the appulse of HD 144206 (FQ = 2), with 95 per cent (2σ) confidence bands.

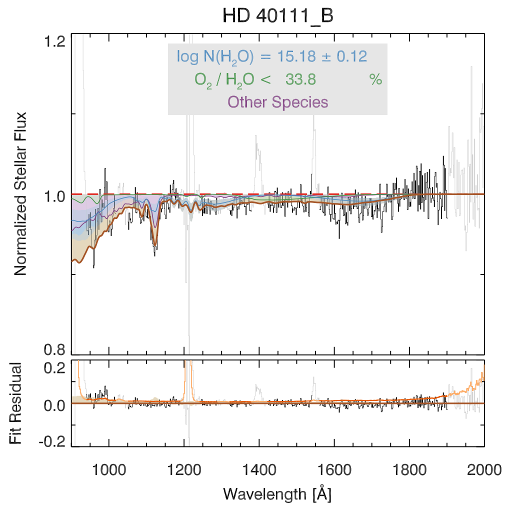

Figure B29. Adopted column densities for the second appulse of HD 40111 (FQ = 3), with 95 per cent (2σ) confidence bands.

This paper has been typeset from a TEX/LATEX file prepared by the author.